Inorganic Chemistry

Article

pubs.acs.org/IC

Structural and Spectroscopic Properties of the Peroxodiferric Intermediate of *Ricinus communis* Soluble Δ^9 Desaturase

Martin Srnec,[†] Tibor András Rokob,[†] Jennifer K. Schwartz,[‡] Yeonju Kwak,[‡] Lubomír Rulíšek,*[,†] and Edward I. Solomon*[,‡]

[†]Institute of Organic Chemistry and Biochemistry, Gilead Sciences & IOCB Research Center, Academy of Sciences of the Czech Republic, Flemingovo náměstí 2, 166 10 Praha 6, Czech Republic

[‡]Department of Chemistry, Stanford University, Stanford, California 94305-5080, United States

Supporting Information

ABSTRACT: Large-scale quantum and molecular mechanical methods (QM/MM) and QM calculations were carried out on the soluble Δ^9 desaturase (Δ^9D) to investigate various structural models of the spectroscopically defined peroxodiferric (**P**) intermediate. This allowed us to formulate a consistent mechanistic picture for the initial stages of the reaction mechanism of Δ^9D, an important diferrous nonheme iron enzyme that cleaves the C−H bonds in alkane chains resulting in the highly specific insertion of double bonds. The methods (density functional theory (DFT), time-dependent DFT (TD-DFT), QM(DFT)/MM, and TD-DFT with electrostatic embedding) were benchmarked by demonstrating that the known spectroscopic effects and structural perturbation caused by substrate binding to diferrous Δ^9D can be qualitatively reproduced. We show that structural models whose spectroscopic (absorption, circular dichroism (CD), vibrational and Mössbauer) characteristics correlate best with experimental data for the **P** intermediate correspond to the μ-1,2-O_2^{2-} binding mode. Coordination of Glu196 to one of the iron centers (Fe_B) is demonstrated to be flexible, with the monodentate binding providing better agreement with spectroscopic data, and the bidentate structure being slightly favored energetically (1−10 kJ mol^{-1}). Further possible structures, containing an additional proton or water molecule are also evaluated in connection with the possible activation of the **P** intermediate. Specifically, we suggest that protonation of the peroxide moiety, possibly preceded by water binding in the Fe_A coordination sphere, could be responsible for the conversion of the **P** intermediate in Δ^9D into a form capable of hydrogen abstraction. Finally, results are compared with recent findings on the related ribonucleotide reductase and toluene/methane monooxygenase enzymes.

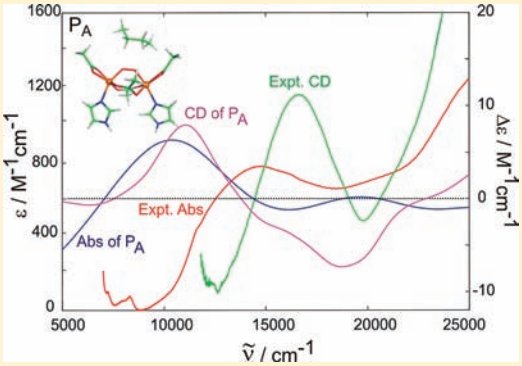

1. INTRODUCTION

Stearoyl-acyl carrier protein Δ^9-desaturase (Δ^9D) is one of the most important enzymes in the fatty-acid metabolism of plants.[1] It catalyzes the oxidation of stearic acid, attached via a thioester link to acyl carrier protein (stearoyl-ACP), to oleoyl-ACP.[1,2] The reaction is stereoselective, yielding the cis configuration of the double bond between the carbons C9 and C10 in the product. Concomitantly, one molecule of dioxygen is reduced to water. The reaction can be summarized as follows:

$$\text{-}CH_2 - CH_2\text{-} + O_2 + 2e^- + 2H^+ \rightarrow \text{-}CH{=}CH\text{-} + 2H_2O \quad (1)$$

After completion of the catalytic cycle, the enzyme function is restored by a two-electron reduction mediated by ferredoxin. Since the C−H bond dissociation energy is about 400 kJ mol^{-1}, a highly reactive intermediate capable of homolytic cleavage of very stable C−H bonds of the substrate is expected to be formed in the active site.

Structurally, Δ^9D consists of two equivalent monomers, each of them containing dinuclear nonheme iron active sites. The catalytic cleft of Δ^9D can be related to the R2 subunit in ribonucleotide reductase (RNR) and to the hydroxylase components of methane mono-oxygenase (MMO) and toluene/*o*-xylene monooxygenase (ToMO) as well as toluene 4-monooxygenase (T4MO).[2−4] Despite a high degree of similarity in the structure of their active sites, the enzymes have different roles: Δ^9D catalyzes dehydrogenation of the aliphatic chain of stearic acid; MMO converts methane to methanol, ToMO and T4MO perform aromatic hydroxylation, and the R2 subunit in RNR promotes homolytic cleavage of the O−H bond in a tyrosine residue. For RNR, the tyrosine then serves as a stable radical storage site for electron transfer from the active site of the second subunit in the course of ribonucleotide reduction. Thus, it appears that reaction mechanisms in these enzymes are extremely fine-tuned.

In spite of many studies exploring catalytic and electronic properties of Δ^9D (e.g., refs 2, 5) a detailed structural and energetic description of the reaction mechanism has not yet been formulated. Experimental observations do, however,

Received: August 18, 2011
Published: February 14, 2012

   dx.doi.org/10.1021/ic2018067 | *Inorg. Chem.* 2012, 51, 2806−2820

Table 1. Experimental Data for the P Intermediate in the Reaction Cycle of Δ^9D[a]

intermediate	ν_s(Fe−O) [cm^{-1}][b]	ν_{as}(Fe−O) [cm^{-1}][c]	ν(O−O) [cm^{-1}][d]	δ [mm s^{-1}][e]	ΔE_Q [mm s^{-1}][f]	ν [cm^{-1}][g]	ε [M^{-1} cm^{-1}][h]	J [cm^{-1}][i]
P in Δ^9D	442[10]	490[10]	898[10]	0.68/0.64[11]	1.90/1.06[11]	14285[10]	1100[11]	<0[16]
P in RNR W48F/D84E	457[15,17]	499[17]	868[15,17]	0.65/0.61[13]	1.73/1.48[13]	14000[18]	1800[18]	−50[13]
P in RNR D84E				0.63/0.63[14]	1.58/1.58[14]	14000[14]	1500[14]	
P in mouse RNR				0.63/0.63[19]	1.73/1.73[19]			
P′ in RNR W48A/Y122F				0.45/0.60[20]	1.53/0.53[20]			

[a]For comparison, spectroscopic parameters of **P** and **P′** RNR intermediates are also shown. [b]ν_s(Fe−O): wavenumber of symmetric Fe−O stretching mode obtained from resonance Raman (rR) spectroscopy. [c]ν_{as}(Fe−O): wavenumber of antisymmetric Fe−O stretching mode (rR). [d]ν(O−O): wavenumber of O−O stretching mode (rR). [e]δ: ^{57}Fe Mössbauer isomer shifts of the dinuclear iron center. [f]ΔE_Q: ^{57}Fe Mössbauer quadrupole splitting of the dinuclear iron center. [g]ν: position of peak maximum in UV−vis spectra. [h]ε: extinction coefficient. For Δ^9D, the value is given per diiron center, while for RNR, this was not clearly stated in the corresponding references. [i]J: exchange coupling constant.

provide a solid framework for a theoretical treatment. It was demonstrated that the resting state of Δ^9D contains oxo-bridged diferric centers in the active site. The four-electron reduction in vitro (two-electron in each monomer) with sodium dithionite gives the diferrous state, which reacts very slowly with dioxygen in the absence of the substrate. Importantly, it was found that substrate binding causes structural and electronic perturbation of the diferrous site activating the enzyme for a reaction with O_2 and results in the formation of a peroxodiferric complex (usually denoted as **P**).[6] Related species have also been identified for RNR, MMO,[2] and in T201 variants of ToMO,[7,8] which suggests that this might be an intermediate involved in the catalytic cycle of Δ^9D. It was also shown that the presence of the substrate shifts the reduction potential of the Δ^9D active site by +106 mV, which implies that structural rearrangement upon substrate binding increases the electron affinity of the dinuclear iron active site.[9]

Although the use of dithionite-reduced enzyme allowed the isolation and characterization of the Δ^9D **P** intermediate, the **P** obtained in this way does not lead to the catalytic reaction. Instead, it decays to the resting μ-oxodiferric complex without the formation of 18:1-ACP;[10] the decay was hypothesized to proceed via release of O_2 from one subunit and subsequent intermonomer transfer of two electrons.[11] It is believed that the sodium dithionite used in the 4e^- reduction of Δ^9D (instead of the catalytically competent ferredoxin)[10] might be responsible for the inhibition of the Δ^9D **P** intermediate, or at least an activating factor arising from the presence of ferredoxin is missing.[12] This is in contrast with the chemistry in RNR, MMO, and ToMO/T4MO, where the dithionite-reduced forms are active for the single-turnover reaction (MMO/ToMO/T4MO requiring the presence of the regulatory proteins).

Several studies addressed the spectroscopy of the Δ^9D **P** intermediate; experimental data concerning the structure of the active site are collected in Table 1. Importantly, the spectroscopic properties of **P** intermediates of Δ^9D and RNR are very similar. Both **P** structures have an antiferromagnetically coupled singlet ground state (Δ^9D: J < 0 cm^{-1}; ref 10; RNR W48F/D84E: J = −50 cm^{-1}; ref 13). They also exhibit a similar absorption band (maximum at 700 nm) of comparable intensity 1100 (Δ^9D) vs 1500 M^{-1} cm^{-1} (RNR D84E)[14] corresponding to a peroxide-to-iron charge-transfer (CT) transition. However, the Mössbauer isomer shifts indicate that ligand fields of both iron centers are equivalent in the RNR **P** structure (0.63/0.63 mm s^{-1})[14] whereas they are slightly different in Δ^9D **P** (0.64/0.68 mm s^{-1}).[10] This observation nicely correlates with the difference in resonance Raman (rR) intensities of the antisymmetric Fe−O mode between RNR and Δ^9D **P** (i.e., very weak in RNR but fairly intense in Δ^9D **P** requiring lower symmetry of the site).[10,15] In addition, rR bands are shifted by approximately 30 cm^{-1} to higher energies in Δ^9D **P** in comparison with RNR **P**, which implies stronger Fe−O bonds and either a stronger O−O bond or a greater Fe−O−O angle.

An important mechanistic issue is whether **P** itself, as formed in vivo, can perform the desaturation of 18:0-ACP to 18:1-ACP or whether it converts to a reactive form for catalysis. Interestingly, such an intermediate (denoted **P′**) has been observed in the RNR W48A/Y122F double mutant; it is likely to be short-lived in wild type RNR.[20] According to the spectroscopic properties of RNR **P′**, both irons are still in the ferric oxidation state; thus the O−O bond remains intact (however, the isomer shifts (δ) are lower and the CT absorption intensity is very low).[20] It is noteworthy that an intermediate with high similarity to **P′** has also been characterized for ToMO,[21] which implies that a **P′**-like form may also be relevant for the Δ^9D chemistry. On the basis of an extensive quantum-chemical study, structural candidates for **P** and **P′** intermediates of RNR were suggested.[22] It was shown that intermediate **P** trapped in the D84E mutant of RNR is a *cis*-μ-1,2 peroxo-bridged closed structure, with the mutated Glu84 coordinated to one of the irons in a bidentate fashion, whereas the corresponding Asp84 carboxylate in the wild type is monodentate. This carboxylate was suggested to either accept a proton or allow water to bind to the open coordination position at Fe (in the latter case, a bridging carboxylate is even more opened); either step leads to a structure consistent with spectroscopic data on RNR **P′**, and further increases the electron affinity of **P** activating it for the subsequent electron transfer step. These pathways would be inhibited by the bidentate coordination of Glu84.

To identify structural and electronic properties of the key structures in the Δ^9D reaction cycle and to establish a starting point for further theoretical mechanistic studies, we now present a detailed computational treatment of the Δ^9D reduced state (Fe(II)−Fe(II) oxidation state) without and with the bound substrate, and of possible peroxodiferric intermediates, including the absence or presence of exogenous H^+ or H_2O. Our main goal is to formulate structural candidates for Δ^9D **P** and, possibly, for an activated Δ^9D **P′**. Several equilibrium structures are therefore identified using combined quantum and molecular mechanical methods (QM/MM). Essential spectroscopic characteristics, such as vibrational frequencies, electronic transitions (absorption and circular dichroism (CD)), and Mössbauer parameters are computed using QM/MM and QM methods (at the DFT or TD-DFT level). The calculations are correlated with experimental spectroscopic data for the **P** intermediate, including new CD data presented here. These studies provide a consistent picture of the possible

dx.doi.org/10.1021/ic2018067 | Inorg. Chem. 2012, 51, 2806−2820

intermediate(s) involved in the initial steps of the O_2 reaction of Δ^9D.

2. EXPERIMENTAL DETAILS

Δ^9D and stearoyl-ACP were generously provided by Prof. Brian Fox from University of Wisconsin-Madison. These proteins were mixed with the glassing agent, glycerol, and converted to **P** by reaction of reduced Δ^9D plus excess (2 equivalent) stearoyl-ACP with dioxygen. Low-temperature absorption spectra were obtained on a Cary-17 spectrophotometer, and low-temperature CD spectra were collected on a JASCO J810 spectropolarimeter, using an S-20 photomultiplier (wavelength range of 900−300 nm, UV−vis region). The collected spectra are included in later figures for comparison to and evaluation of calculated absorption and CD data using different possible structural models.

3. COMPUTATIONAL DETAILS

3.1. Combined Quantum Mechanical and Molecular Mechanical (QM/MM) Calculations. The QM/MM calculations were carried out using the COMQUM program.[23,24] Currently, it combines Turbomole 5.7[25] for the QM part with AMBER 8[26] and the Cornell force field[27] for the MM part. Employing the ONIOM-like approach,[28] the protein and solvent are divided into three subsystems: the QM region (system 1) contains the most interesting atoms and is relaxed by QM/MM forces. System 2 consists of all residues within the defined distance from any atom in system 1 (R = 10 Å in this study) and is relaxed by a full MM minimization in each step of the QM/MM geometry optimization. Finally, system 3 contains the remaining part of the protein and surrounding solvent molecules and is kept fixed at the original (crystallographic) positions. In the quantum chemical calculations, the QM system is represented by a wave function, whereas all other atoms are represented by an array of partial point charges, one for each atom, taken from the Amber libraries. Thereby, the polarization of the quantum system by the surroundings is included in a self-consistent manner. In the MM calculations of the QM/MM forces and energies, all atoms are represented by the Amber force field. When there is a bond between systems 1 and 2 (a junction), the quantum region is truncated by hydrogen atoms, the positions of which are linearly related to the corresponding carbon atoms in the full system (the hydrogen link approach).[23,29] To avoid overpolarization of the quantum system, point charges on atoms in the MM region bound to junction atoms are set to zero and the remaining charges on the truncated amino acid are adjusted to keep the fragment neutral. The actual charges used for all atoms can be found in the sample PDB file in the Supporting Information (last column).

The total energy is calculated as

$$E_{tot} = E_{QM} + E_{MM123} - E_{MM1} \quad (2)$$

Here, E_{QM} is the QM energy of the quantum system truncated by the hydrogen atoms, including the point charges in the Hamiltonian, but excluding their self-energy. E_{MM1} is the MM energy of the quantum system, still truncated by hydrogen atoms, but without any electrostatic interactions. Finally, E_{MM123} is the classical energy of all atoms in the system with normal atoms at the junctions and with the charges of the quantum system set to zero (to avoid double-counting of the electrostatic interactions). The calculated forces are the gradient of this energy, but owing to the presence of junction atoms which are not the same in the QM and MM123 systems, they have to be computed using the chain rule.

3.2. Protein and System Setup. All calculations reported in this work are based on the crystal structure of recombinant homodimeric Δ^9 stearoyl-acyl carrier protein desaturase (650 amino acids), the archetype of the soluble plant fatty acid desaturases obtained at the resolution of 2.4 Å (Protein Data Bank accession code 1AFR).[30] The reaction was assumed to take place only in the active site of one monomer, whereas the second site was assumed to be a spectator in $Fe^{II}Fe^{II}$ oxidation state which was chosen arbitrarily and conserved throughout the study. We consider this choice as a plausible approximation (owing to the ∼25 Å distance between the two diiron centers) despite the fact that **P** may form in both units of the dimer.[11]

Hydrogen atoms were added by the *leap* module of the AMBER program, assuming that all Asp and Glu residues are negatively charged and all Lys and Arg residues are positively charged. For each monomer, the protonation states of the His residues were determined by a study of the hydrogen-bonding pattern, the surroundings, and the solvent exposure of each residue: His25, 213, 281 were assumed to be protonated on the N^{δ} atom, His146, 232 on the N^{ϵ} atom, and the remaining eight histidines (His30, 54, 203, 268) at both nitrogen atoms, thus bearing a positive charge (residues are numbered according to the 1AFR crystal structure). This assignment led to an overall charge of −5 for the protein (including −1 charge on the substrate). It can be mentioned that the crystal structure was determined at pH 6.5.

Since there is no X-ray structure of the [protein···substrate (stearoyl-ACP)] complex available, a simplified substrate model (CH_3-$(CH_2)_{16}$-COO-phosphopanteteine linker capped by CH_3 group instead of ACP) was manually docked into the substrate entrance channel in Δ^9D in a way that the C10 and C9 carbons were positioned in the vicinity of the dinuclear iron center. In total, seven initial positions of the substrate in the Δ^9D active site were prepared and subjected to the simulated annealing (vide infra).

The protein−substrate complex was then solvated in a shell of explicit TIP3P water molecules with a thickness of 10 Å which resulted in an addition of approximately 6840 water molecules yielding a total number of ∼32090 atoms in the simulations. The positions of all hydrogen atoms, added water molecules, and substrate were first minimized and then equilibrated for 300 ps using a simulated annealing protocol (heating the system to 370 K and cooling it slowly down to 0 K), keeping all remaining atoms at the original positions.

Charges for the two Fe ions and their ligands in the MM region (i.e., the "spectator" active site in the second monomer) were taken from QM calculations. The QM electrostatic potential was calculated in 10000 random points up to 8 Å from the molecule. The charges were then fitted to reproduce these potentials, using a Boltzmann weighting for points close to the active-site model. In the fit, it was ensured that the total charge and dipole moment were exactly reproduced, whereas the fit was restrained to reproduce also the quadrupole and octupole moment (the CHELP-BOW procedure).[31] The resulting charges are collected in the sample PDB file deposited as Supporting Information.

System 1 (the quantum region) consists of 60−70 atoms (including two iron ions, four acetates, two imizadoles, one butane, and possibly one (metal-bound) solvent molecule and one O_2 species). It is depicted in Figure 1.

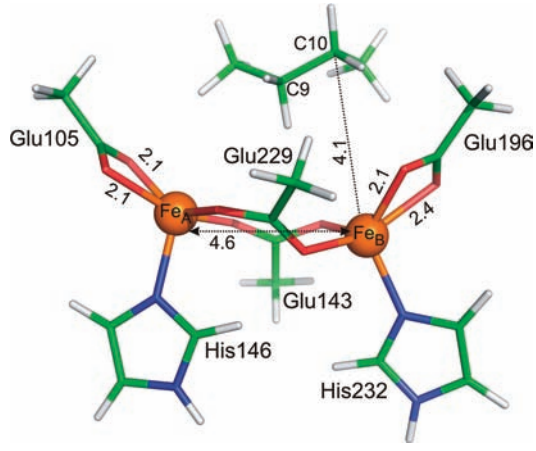

Figure 1. Quantum system for the reduced [Δ^9D···substrate] complex. The distances are in Å.

3.3. Treatment of the Quantum Region. Density functional theory (DFT) calculations were employed to treat the quantum region in the QM/MM studies, mostly carried out using the Turbomole (versions 5.7 and 6.1)[25] and ORCA program packages.[32]

dx.doi.org/10.1021/ic2018067 | Inorg. Chem. 2012, 51, 2806−2820

All the QM/MM geometry optimizations employed the BP[33−35] functional and the def2-SVP basis set[36] for all atoms, unless explicitly noted. Calculations with this functional were further expedited by expanding the Coulomb integrals in an auxiliary basis set employing the resolution-of-identity (RI-J) approximation.[37,38] Spin populations are also reported from this level of theory. Single point QM/MM energies were obtained using the B3LYP[33,35,39,40] functional and the def2-TZVP basis set,[36] if not stated otherwise.

Electronic and Mössbauer spectroscopic properties were calculated using the QM/MM geometries, with the protein environment being included as an array of point charges (electronic embedding). Excitation energies, oscillator (f) and rotatory (R) strengths[41] (with molar extinction coefficient given per diiron center) were computed using time-dependent DFT (TD-DFT) at the B3LYP/def2-TZVP level. Mössbauer isomer shifts (δ) were estimated from fitted plots of δ versus calculated electron densities (ρ) at iron centers, $\delta = a(\rho - b)$ (where a and b are empirical parameters), according to approaches discussed by Jensen et al.[22] (Approach 1) and Neese[42] (Approach 2). In Approach 1, the QM/MM electron densities at iron centers were obtained at the same level as used for geometry optimization (BP/def2-SVP), while in Approach 2, the same functional in conjunction with the CP(PPP) basis set[42] on the iron atoms and the DZP basis set[43] on the other atoms was used. Approach 2 was also used to obtain an estimate of the quadrupole splitting (ΔE_Q). However, we consider the ΔE_Q values only as qualitative, because of relatively large errors in the calculation (up to 0.3−0.5 mm s^{-1}, according to ref 42.). The error bar of Approaches 1 and 2 in the prediction of δ is estimated to be approximately 0.1 mm s^{-1} (refs 22, 42).

Harmonic frequencies of normal vibrational modes were calculated for a small in vacuo cluster model corresponding to the QM part of the QM/MM calculations, reoptimized with the atoms neighboring the junction atoms fixed (N^{δ} atoms of both His232 and His146 and C atoms of Glu105, Glu143, Glu196, and Glu229). The BP/def2-SVP level of theory (the same as used for the QM/MM geometry optimizations) was employed.

The antiferromagnetically coupled electronic states were obtained using the spin-flip broken-symmetry DFT approach.[44] All equilibrium geometries as well as ground-state and excitation energies reported were obtained for antiferromagnetically coupled high-spin iron centers, yielding an $M_s = 0$ state in both the **P** intermediate and the resting state.[1,2] The values of exchange coupling constants (J) were calculated according to Yamaguchi et al.[45] at the same level of theory as the Mössbauer parameters using Approach 2 (BP functional, CP(PPP) basis set on Fe, DZP on the other atoms, protein environment as point charges).

3.4. Cluster Calculations. In addition to the QM/MM treatment, the diferrous active site and various structures of the intermediates were also studied in the absence of the explicit protein environment, as a cluster model including first and second-shell residues. The results from these calculations are in good agreement with the full QM/MM treatment; further details about them are provided in the Supporting Information.

4. RESULTS AND DISCUSSION

4.1. Effect of Substrate Binding on the Geometry of the Active Site in the Reduced State. As shown previously,[6] analysis of CD and variable-temperature, variable-field magnetic CD (VTVH MCD) spectra of the substrate-free and substrate-bound diferrous Δ^9D provided strong evidence for a change in the ligand field of one of the two irons upon substrate binding, which correlated with an increased reactivity of the diferrous active site toward dioxygen. In this study, we use this structural and spectroscopic effect of the substrate on the active site for testing the capability of our QM/MM models to predict spectral effects of subtle structural changes in the coordination sphere of the irons.

As shown in Figure 2, the experimental and calculated CD spectra of substrate-free Δ^9D exhibit two d-d transitions

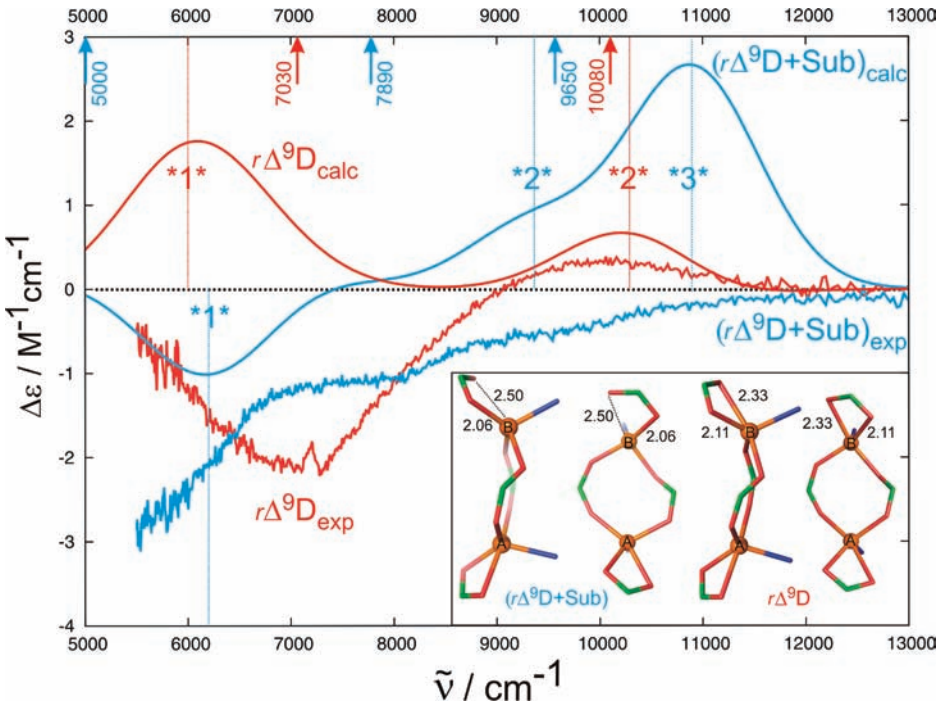

Figure 2. Calculated and experimental CD spectra for the reduced (diferrous) substrate-free Δ^9D ($r\Delta^9$D, in red) and the reduced substrate-bound Δ^9D ($r\Delta^9$D+Sub, in blue). Positions of the most intense transitions are also displayed (dotted lines: TD-DFT ($R > 10^{-4}$ a.u.); arrows: experimental CD); the Kohn−Sham orbitals involved in these transitions are depicted in Supporting Information, Figure S4. Spectra were calculated for $M_S = 0$ state with TD-DFT(B3LYP)/def2-TZVP + point-charges, using the QM/MM geometries. Bands were modeled using Gaussian functions with an arbitrarily chosen bandwidth (fwhm) of 1500 cm^{-1}. Note that the Fe_B-O_{Glu196} distance in $r\Delta^9$D+Sub is restrained at 2.5 Å as depicted in the inset. Experimental spectra were taken from ref 6.

dx.doi.org/10.1021/ic2018067 | Inorg. Chem. 2012, 51, 2806−2820

(calculated at 5982 and 10265 cm^{-1} vs experimental 7030 and 10080 cm^{-1}) reflecting the very similar distorted-square-pyramidal ligand-field arrangements around the two ferrous centers.

In the QM/MM model of substrate-bound Δ^9D, the active site is only slightly perturbed relative to the substrate-free model; the most noticeable change in the geometry is an elongation of the Fe_B-O_{Glu196} bond from 2.3 to 2.4 Å. Such a perturbed structure shows three d-d transitions (one negative at 6191 cm^{-1} and two positive at 10254 and 10819 cm^{-1}), which correlates with three CD bands in the experimental spectrum, but the splitting of the two at the higher energy in the TD-DFT calculated CD is only 600 cm^{-1} in comparison with the experimental value of 2620 cm^{-1}. Thus, in the CD spectrum simulated by Gaussian functions with fwhm values of 1500 cm^{-1} (experimental fwhm-s are 1500−2200 cm^{-1}; ref 6.), these two transitions overlap producing a single absorption band. Elongating and restraining the Fe_B-O_{Glu196} bond to 2.5 Å, we obtain a substrate-bound Δ^9D model that is characterized by three distinguishable d-d transitions, in agreement with experiment (6199, 9369, and 10899 cm^{-1} calculated vs 5000, 7030, and 9650 cm^{-1} experimental). It is noteworthy that this restrained QM/MM structure is only marginally (~1 kJ mol^{-1}) less stable than the fully optimized QM/MM model of substrate-bound Δ^9D. In addition to the correlation of the TD-DFT calculations with the experimental CD spectrum, the coordination arrangements of the two ferrous ions in the restrained QM/MM structure conform to the geometry predicted from the experiment and ligand-field theory (ref 6.), that is, one of the two irons remains five-coordinate with the distorted square pyramid coordination, while the other iron distorts to become four-coordinate. This agreement corroborates that our QM/MM model can provide reasonable predictions to relate structural and spectroscopic parameters. This starting structure was used for calculations of O_2 binding to generate the **P** structures below.

4.2. Geometric and Energetic Characterization of Structural Models of the Peroxo Intermediate in the Absence of a Water Molecule or Proton. Large-scale QM/MM calculations were used to define the mode of peroxide coordination to the two irons in Δ^9D **P** and elucidate the possible existence of an energetically accessible, more reactive Δ^9D **P′** intermediate. From many initial structures, four relevant local minima were obtained, denoted as $\mathbf{P_A}$, $\mathbf{P_B}$, $\mathbf{P_C}$, and $\mathbf{P_D}$ and depicted in Figure 3A. The energetically most stable $\mathbf{P_A}$ and $\mathbf{P_B}$ isomers both correspond to μ-1,2-peroxo complexes; they differ in the coordination of other ligands to the iron centers. In $\mathbf{P_A}$, both irons are six-coordinate (6C,6C). As the analysis of VTVH MCD experiments carried out for the fully reduced Δ^9D-substrate complex suggested a monodentate coordination of the terminal Glu ligand to Fe_B,[6] we attempted to find the corresponding oxygenated (6C,5C) isomer. However, the QM/MM calculations failed to identify a local minimum resembling the (6C,5C) structural arrangement. Therefore, the (6C,5C) model ($\mathbf{P_B}$) was prepared by applying restraints on the interatomic Fe_B-O_{Glu196} distance using harmonic potentials with minima at either 2.5 or 3.5 Å and a force constant of 9375 kJ mol^{-1} $Å^{-2}$ (1.0 au) during the geometry optimization. The resulting $\mathbf{P_B}$(6C,5C) structure is only marginally higher in energy (2 and 9 kJ mol^{-1} for restraints at 2.5 and 3.5 Å, respectively) than the $\mathbf{P_A}$(6C,6C) isomer, indicating a flat potential energy surface for the transition from bidentate to monodentate coordination of the Glu residue. A likely explanation for the absence of a corresponding (6C,5C) local minimum in the calculations is an insufficient stabilization of the terminal Glu in a monodentate mode by the neighboring second-shell Trp139 residue. Moreover, the effects of the bound substrate on large conformational motions of the protein were not studied, and therefore the existence of conformational changes stabilizing this (6C,5C) structure cannot be excluded. On the other hand, we found local minima for different coordination modes of the oxygen ligand, namely, μ-η^2:η^1-type isomers $\mathbf{P_C}$ and $\mathbf{P_D}$. However, these structures are disfavored by 41 and 62 kJ mol^{-1} with respect to the most stable μ-1,2 $\mathbf{P_A}$ structure (see Figure 3A and Table 2). We note in passing that $\mathbf{P_C}$ behaves very similarly to $\mathbf{P_A}$ in that it also requires a quite small amount of energy to convert Glu196 to monodentate, but that monodentate structure does not exist as a minimum in our calculations either.

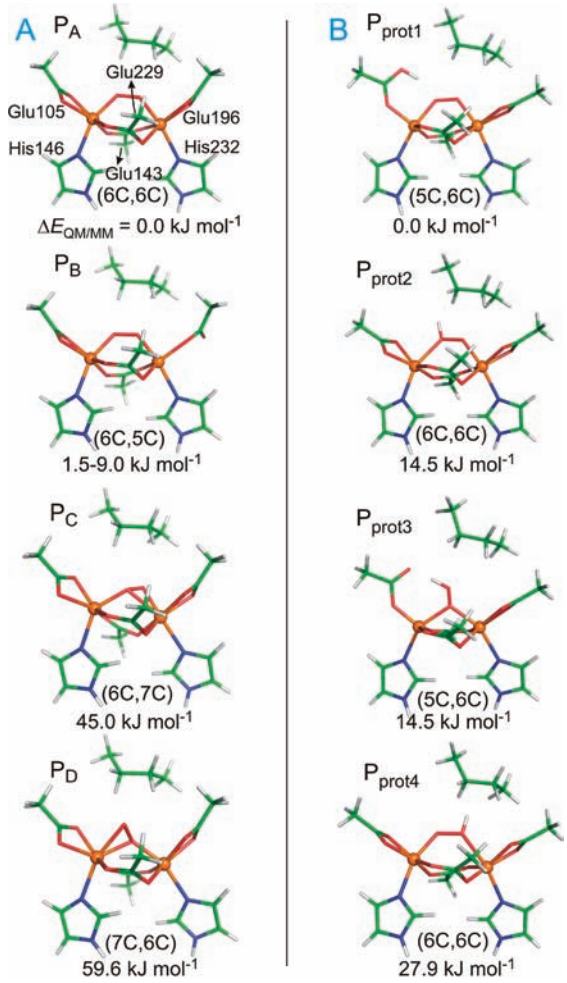

Figure 3. Structural models for the Δ^9D peroxo intermediate without H^+/H_2O (A) and with H^+ (B), together with their calculated relative energies. Selected geometric parameters for the QM/MM models are displayed in Supporting Information, Table S3.

4.3. Spectroscopic Characterization of the Peroxo Intermediate in the Absence of Water and Proton. *Electronic Spectroscopy* . As indicated in Table 2, the exchange coupling between the two high-spin iron ions was found to be negative in all model structures (i.e., all of these structures are predicted to have antiferromagnetic coupling). *J*-coupling constants in both μ-1,2 $\mathbf{P_A}$ and $\mathbf{P_B}$ seem too negative (~ −110 cm^{-1}) in comparison with J = −50 cm^{-1} of the

dx.doi.org/10.1021/ic2018067 | *Inorg. Chem.* 2012, 51, 2806−2820

Table 2. Possible Candidates of the P Intermediate in the Absence and Presence of a Water Molecule or a Proton: Ligand Field Structures, Spin Populations, Exchange Coupling Constants, and QM/MM Energetics[a]

	ligand field[b] Fe_A:Fe_B	spin population Fe_A;O_A:Fe_B;O_B	J (cm^{-1})	ΔE_{MM}[c]	$\Delta E_{QM\text{-}vac}$[d]	$\Delta E_{QM/MM}$[e]
P						
P_A	DO:DO	−3.90;−0.19:3.90;0.17	−114	0.0	0.0	0.0
P_B (2.5 Å)[f]	DO:TB	−3.90;−0.19:3.90;0.18	−113	1.4	5.9	1.5
P_B (3.5 Å)[f]	DO:TB	−3.92;−0.19:3.89;0.19	−106	22.4	23.5	9.0
P_C	SP:SP	−4.00;−0.09:3.94;0.24	−56	18.8	17.3	45.0
P_D	SP:SP	−3.95;0.02:3.90;0.03	−63	15.7	44.0	59.6
P with H^+						
P_{prot1}	TB:DO	3.91;0.19:−3.92;−0.14	−94	0.0	0.0	0.0
P_{prot2}	DO:DO	4.11;0.01:−4.02;−0.26	−26	19.4	40.2	14.5
P_{prot3}	SP:DO	4.03;−0.01:−4.05;−0.07	−27	12.9	3.0	14.5
P_{prot4}	DO:DO	−4.02;−0.31:4.07;−0.01	−20	16.7	41.7	27.9
P with H_2O						
P_{w1}	DO:DO	−3.94;−0.17:3.93;0.19	−96	0.0	0.0	0.0
P_{w2} (2.5 Å)[f]	DO:TB	−3.94;−0.17:3.92;0.19	−96	0.1	6.6	1.8
P_{w2} (3.0 Å)[f]	DO:TB	−3.95;−0.17:3.91;0.20	−93	7.9	12.4	2.6
P_{w2} (3.5 Å)[f]	DO:TB	−3.95;−0.17:3.91;0.20	−90	17.2	17.5	7.9
P_{w3}	DO:DO	3.95;−0.07:−3.73;−0.19	−89	2.2	38.8	48.8
P_{w4}	DO:DO	−3.66;−0.18:3.88;0.04	−70	5.8	35.6	38.0
P_{w5}	DO:DO	−3.94;−0.18:3.93;0.20	−85	62.0	−23.9	36.9
P_{w6}	DO:SP	−3.91;−0.05:3.85;0.28	−99	25.1	5.2	50.6
P_{w7}	DO:DO	−3.90;−0.20:3.90;0.16	−122	12.2	−1.1	56.3
P_{w8}	SP:DO	−3.87;−0.26:3.91;0.09	−97	−22.2	−16.7	25.5
P_{w9}	DO:DO	−3.94;−0.20:3.91;0.16	−103	4.0	−15.2	41.9
P_{w10}	SP:DO	−3.94;−0.17:3.93;0.19	−77	−11.9	18.1	68.0
P_{w11}	SP:DO	3.80;0.15:−3.89;−0.14	−82	−21.3	42.1	100.6
P_{w12}	DO:SP	−3.98;0.00:4.00;−0.02	+40	20.5	41.8	50.1
P_{w13}	SP:SP	−3.98;−0.02:3.95;0.26	−46	7.6	12.3	78.2

[a]All energy values are in kJ mol^{-1}. [b]DO, distorted octahedral; SP, square pyramidal; TB, trigonal bipyramidal. [c]MM energy differences in Systems 2 and 3 (nonelectrostatic MM energy). [d]In vacuo QM energy differences in System 1. [e]Total QM/MM energy difference. The energy difference contribution arising from electrostatics in Systems 2 and 3 as well as their interaction with System 1 can be deduced according to the relation: $\Delta E_{QM/MM} - (\Delta E_{QM\text{-}vac} + \Delta E_{MM})$. [f]Restrained Fe_B-O_{Glu196} distance.

μ-1,2 **P** RNR.[13] It should be stressed, however, that the absolute values of the calculated antiferromagnetic J's are expected to be overestimated since the BP functional tends to stabilize the low-spin relative to the high-spin electronic structure (see, for example, ref 46, and citations therein).

The experimental low-temperature absorption spectrum of **P** in Δ^9D is shown in Figure 4. Simulated electronic absorption spectra for the above-discussed structural candidates ($\mathbf{P_A}$, $\mathbf{P_B}$, $\mathbf{P_C}$, and $\mathbf{P_D}$) for the **P** intermediate were obtained using TD-DFT(B3LYP)/def2-TZVP calculations in the field of surrounding point charges at the QM/MM equilibrium geometries. The calculated absorption spectra for the *cis*-μ-1,2-peroxodiferric complexes (structures $\mathbf{P_A}$ and $\mathbf{P_B}$) are in reasonable agreement with the experimental absorption spectrum (with respect to the position and the shape of the intense ligand−metal charge transfer (LMCT) band), whereas the band shapes of the $\mathbf{P_C}$ and $\mathbf{P_D}$ structures (side-on μ-η^2:η^1 complexes) significantly differ (see Figure 4 for $\mathbf{P_A}$, and in Supporting Information, Figure S6 for the rest). Therefore, on the basis of the calculated energy and spectrum, $\mathbf{P_C}$ and $\mathbf{P_D}$ structures do not correspond to the **P** intermediate characterized spectroscopically.[10] The most characteristic and intense LMCT transition, $\pi^*(O_2^{2-}) \rightarrow d(Fe^{III})$, lies experimentally at 14285 cm^{-1} (see Table 1 and Figure 4), while the calculated values are 11260 cm^{-1} ($\mathbf{P_A}$) and 11250 cm^{-1} ($\mathbf{P_B}$ with Fe_B-O_{Glu196} restrained to 3.5 Å). The computed spectra of $\mathbf{P_A}$ and $\mathbf{P_B}$ are also consistent with the simulated spectrum for the **P** intermediate of RNR (structure taken from ref 22). The difference between the calculated and experimental data is within the expected error bar of the TD-DFT method (~3000 cm^{-1}).[47] In addition, as discussed by Besley and Robinson,[48] the B3LYP functional is known to underestimate energies of charge-transfer excited states, which is fully in line with our observation. It can be mentioned that more sophisticated calculations, such as CASPT2 or MRCI, cannot be applied to these systems as they are prohibitively expensive.

As shown in Figure 4, important insight into the composition of the broad experimental CT absorption band is provided by the corresponding low-temperature CD spectrum, which clearly shows that the LMCT band actually consists of two transitions having opposite CD signs and maxima at ~12500 and ~16000 cm^{-1}. Thus, the position of the LMCT absorption maximum corresponds approximately to the inflection point between the two maxima of the negative and positive CD bands. Both transitions are assigned as peroxide $\pi^*_v \rightarrow d_\pi(Fe^{III})$ charge transfer excitations (π^*_v is the valence orbital on peroxide involved in π bonding to Fe). These are the symmetric and antisymmetric combinations of the CT transitions to the two Fe^{III} centers in the bridged structure. The TD-DFT CD spectrum of $\mathbf{P_A}$ (and also $\mathbf{P_B}$, see Supporting Information, Figure S7) possesses similar features to the experimental CD spectrum of **P** (Figure 4). Importantly, it was found that the calculated CD profile is only slightly affected by the chiral protein environment (cf. Supporting Information, Figure S9). Therefore, the

dx.doi.org/10.1021/ic2018067 | Inorg. Chem. 2012, 51, 2806−2820

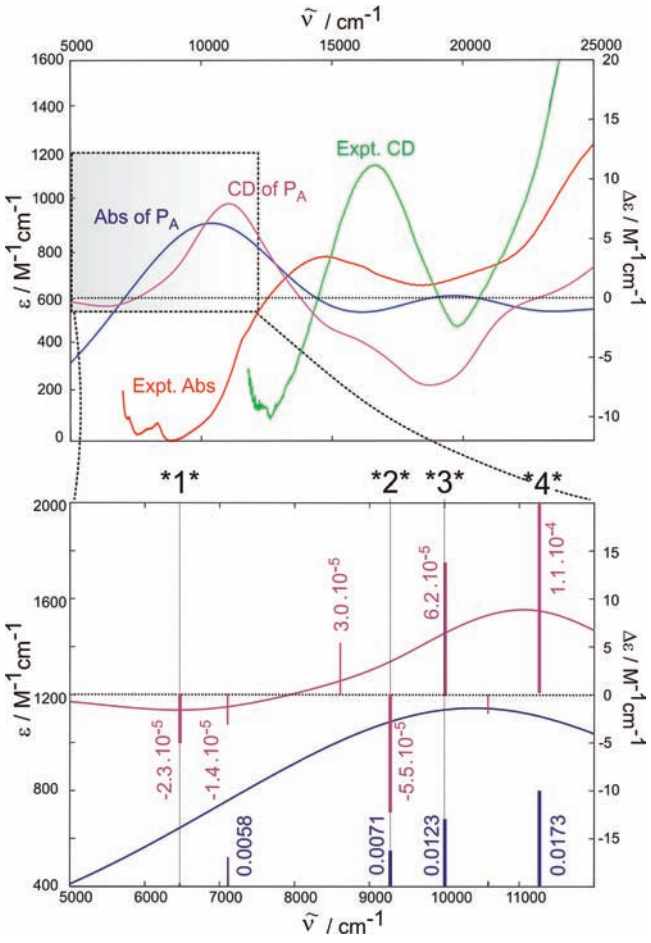

Figure 4. Calculated electronic absorption and CD spectra of the $\mathbf{P_A}$ structure compared with the corresponding experimental spectra of Δ^9D intermediate **P**. The spectra of $\mathbf{P_A}$ were calculated for $M_S = 0$ with TD-DFT(B3LYP)/def2-TZVP + point-charges at the QM/MM equilibrium geometry. Bands were modeled using hybrid Gaussian/Lorentzian line shape (both with relative weight of 0.5) with an arbitrarily chosen bandwidth (fwhm) of 7000 cm^{-1} (Abs) and 3000 cm^{-1} (CD). Values of oscillator (f) and rotatory (R) strengths of transitions (velocity representation) are provided as numbers next to the corresponding peaks (in blue and violet color, respectively). R is in atomic units. The Kohn–Sham orbitals involved in the most characteristic transitions are depicted in Figure 5.

CD spectra of QM/MM (or QM) models can serve as a direct probe of the local active-site asymmetry of metalloproteins.

In the 5000–12000 cm^{-1} region, the TD-DFT CD profile of $\mathbf{P_A}$ (and $\mathbf{P_B}$) has a derivative shape with maxima at ~6500 and ~11100 cm^{-1} (shifted by ~3000–5000 cm^{-1} to lower energy relative to the corresponding experimental transitions). This shape reflects four major contributions (two positive and two negative), which arise from electronic excitations involving the Kohn–Sham orbitals depicted in Figure 5. It can be seen that all four transitions have LMCT $\pi^*(O_2^{2-}) \rightarrow d(Fe^{III})$ character with contributions from different d acceptor orbitals on both irons.

We note that in the higher energy region (above 20000 cm^{-1} in the experimental CD), the measured spectrum has contributions from both the $\pi_\sigma^*(O_2^{2-}) \rightarrow d_\sigma(Fe^{III})$ and $COO^- \rightarrow Fe^{III}$ CT transitions. On the other hand, the TD-DFT transitions in the range of 15000–28000 cm^{-1} are characterized as $\pi^*(O_2^{2-}) \rightarrow d(Fe^{III})$ with significant admixture of $p_{O,Glu}$ orbitals to acceptor $d(Fe_A$ and/or $Fe_B)$ orbitals.

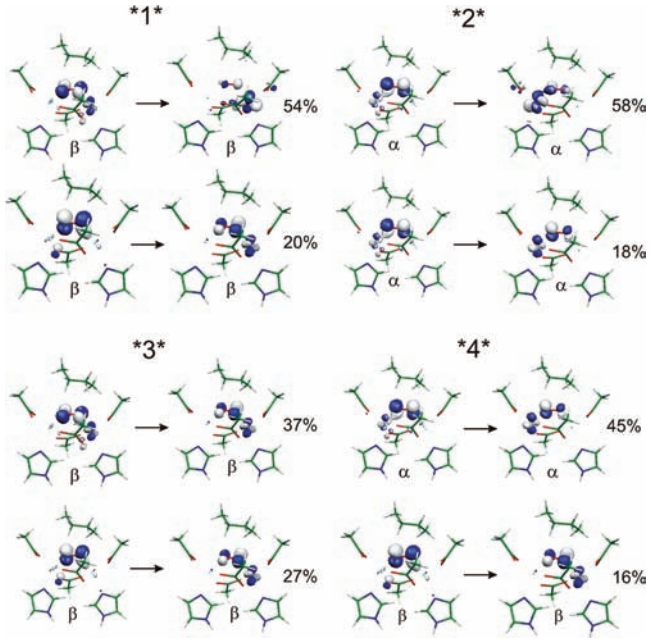

Figure 5. Kohn–Sham orbitals involved (with contribution >15%) in the most characteristic electronic absorption and CD transitions of $\mathbf{P_A}$. For the corresponding spectral peaks, see Figure 4.

Considering all information obtained from electronic spectroscopy, it can be concluded that the calculated absorption and CD spectra of $\mathbf{P_A}$ and $\mathbf{P_B}$ intermediates make both structures viable candidates for the **P** intermediate in Δ^9D. For sake of completeness, the calculated CD spectra of all four structures studied are given in Supporting Information, Figure S7.

Mössbauer Isomer Shifts. The calculated Mössbauer isomer shifts obtained from Approach 1 are listed in Table 3; isomer shifts and quadrupole splittings using Approach 2 are given in Supporting Information, Table S4. In general, there is a consistency between values obtained from Approaches 1 and 2, apart from values from Approach 2 being usually systematically shifted by ~0.06 mm s^{-1} toward higher values. As can be inferred from the calculated values, all structures are characterized by nonequivalent iron sites, including the $\mathbf{P_A}$ model with (6C,6C) coordination sphere. Experimental isomer shifts and the difference in quadrupole splittings between the two ferric ions were determined to be 0.64/0.68 mm s^{-1} and 0.84 mm s^{-1}, respectively, which is consistent with values calculated for both the $\mathbf{P_A}$ and the $\mathbf{P_B}$ structures. Also, the calculated values for the $\mathbf{P_A}$ structure predict slightly more equivalent iron sites than the experimental values obtained for the Δ^9D **P** intermediate, whereas the $\mathbf{P_B}$ structure with a restrained Fe_B-O_{Glu196} distance of >3 Å exhibits slightly more asymmetry than experiment. As expected, along the $\mathbf{P_A} \rightarrow \mathbf{P_B}$ transition pathway the difference in isomer shifts increases and for $d(Fe_B\text{-}O_{Glu196})$ = 3.5 Å we obtained $\delta(Fe_A)/\delta(Fe_B)$ values of 0.68/0.58 mm s^{-1}. Considering the fact that $|\delta(Fe_A) - \delta(Fe_B)|$ values for $\mathbf{P_C}$ and $\mathbf{P_D}$ are larger than 0.07 mm s^{-1} (cf. experimental 0.04 mm s^{-1}), we exclude these models as possible candidates for **P** Δ^9D.

Vibrational Spectroscopy. Approximations used in the frequency calculations (e.g., harmonic approximation, infinite mass of fixed atoms in the cluster model during the diagonalization of the Hessian matrix, limited accuracy of electronic structure methods) preclude a straightforward choice among similar structural candidates by direct quantitative

dx.doi.org/10.1021/ic2018067 | Inorg. Chem. 2012, 51, 2806–2820

Table 3. Calculated Mössbauer Isomer Shifts of the Structural Candidates for the P Intermediate[a] for the $M_S = 0$ Antiferromagnetically Coupled Ground State[b]

	$\delta(Fe_A)$	$\delta(Fe_B)$
P		
P_A	0.66	0.69
P_B (2.5 Å)[c]	0.67	0.66
P_B (3.5 Å)[c]	0.68	0.58
P_C	0.61	0.75
P_D	0.73	0.66
P with H^+		
P_{prot1}	0.57	0.60
P_{prot2}	0.57	0.64
P_{prot3}	0.47	0.62
P_{prot4}	0.60	0.56
P with H_2O		
P_{w1}	0.67	0.68
P_{w2} (2.5 Å)[c]	0.67	0.64
P_{w2} (3.0 Å)[c]	0.68	0.58
P_{w2} (3.5 Å)[c]	0.68	0.57
P_{w3}	0.78	0.74
P_{w4}	0.77	0.79
P_{w5}	0.67	0.81
P_{w6}	0.62	0.62
P_{w7}	0.77	0.71
P_{w8}	0.53	0.65
P_{w9}	0.76	0.66
P_{w10}	0.35	0.70
P_{w11}	0.44	0.66
P_{w12}	0.77	0.70
P_{w13}	0.60	0.64

[a]In the absence and presence of a water molecule or a proton. [b]Using Approach 1 as described in the Computational Details. [c]Values in parentheses refer to the restrained Fe_B-O_{Glu196} distance in the model.

comparison of the calculated and experimental frequencies. However, we assume that comparison of the frequency differences between the two Fe−O stretching modes may be more reliable because of the expected error cancellation (the two modes lie in the same frequency region and involve essentially the same atoms). The calculated symmetric and antisymmetric Fe−O modes are schematically depicted in Supporting Information, Figure S10. It should be mentioned that in an ideal symmetric case, the antisymmetric Fe−O mode would be expected to have vanishing rR intensity. Its observed appearance in the experimental spectrum indicates a somewhat lower symmetry, lending partial localized character (Fe_A-O and Fe_B-O) and thus nonvanishing rR activity to both the symmetric and antisymmetric Fe−O modes.

The calculated data are summarized in Table 4. It can be seen that $\Delta\nu_{Fe-O}$ ($\Delta\nu_{Fe-O} = \nu_{as,Fe-O} - \nu_{s,Fe-O}$) calculated for the $\mathbf{P_A}$ and $\mathbf{P_B}$ structures (47 and 46 cm^{-1}, respectively) are in excellent agreement with the experimental value of 48 cm^{-1}. Also, the $^{16}O_2/^{18}O_2$ isotope shift in the Fe−O and O−O frequencies agrees well with the experimental (rR) data for the **P**. On the contrary, the $\mathbf{P_D}$ structure exhibits much larger deviations from the experimental values ($\Delta\nu_{Fe-O}$ = 246 and $\Delta\nu_{Fe-O}(\Delta^{18}O)$ = +31 cm^{-1}) and while no local minimum was found for the $\mathbf{P_C}$ structure in the cluster model, structural similarity of $\mathbf{P_C}$ and $\mathbf{P_D}$ suggests similar deviations.

We may conclude that the QM/MM calculations carried out for the structural models of the observed **P** intermediate in Δ^9D in the absence of a water molecule have convincingly shown that both side-on μ-η^2:η^1 $\mathbf{P_C}$ and $\mathbf{P_D}$ structures have spectroscopic data inconsistent with experiments on Δ^9D **P**, and they are furthermore at too high energy to be considered either as **P** or **P′**. On the other hand, spectroscopic properties of the significantly more stable μ-1,2 (6C,6C) $\mathbf{P_A}$ and (6C,5C) $\mathbf{P_B}$ structures are in good agreement with the experimental data, which makes them viable structural candidates for the **P** intermediate in Δ^9D.

4.4. Geometric and Energetic Characterization of Protonated Models of the Peroxo Intermediate. Structures with an additional proton in the dinuclear active site (i.e., bound to one of the ligands including peroxide) represent a group of possible candidates for the **P** or **P′** intermediate. In these structures, two different proton sources can be envisaged. The first is the second-shell His203 residue whose N^{ε} and N^{δ} sites are both protonated in the initial QM/MM and QM-only structures. The relevance of the protonated state for His203 was inferred from its hydrogen-bond network in the Δ^9D crystal structure (Supporting Information, Figure S5). The second source of the proton can be the solvent. Disregarding the proton source, the protonated QM/MM models of peroxo Δ^9D were prepared by addition of an exogenous proton into the active site (QM system).

The putative existence of protonated His203 (see Supporting Information, Figure S1) and its potential to act as a proton source clearly imply the possible protonation of the neighboring terminal Glu105 ligand of Fe_A. This causes a structural rearrangement of the Fe_A center from distorted octahedral to trigonal bipyramidal, with the Glu105 carboxylate becoming monodentate. This gives rise to the $\mathbf{P_{prot1}}$ QM/MM model (see Figure 3B). As another possibility, structures bearing the extra proton on the peroxide moiety were considered ($\mathbf{P_{prot2}}$, $\mathbf{P_{prot3}}$, $\mathbf{P_{prot4}}$).

Among these isomers, the most stable structure is μ-1,2 (5C,6C) $\mathbf{P_{prot1}}$ with the proton on the Glu105 oriented toward and H-bonding to the peroxide bridge. The QM/MM calculations predict that the direct proton transfer from Glu105 to the intact μ-1,2 peroxide moiety is not favorable; a conversion of the peroxide to the μ-1,1 coordination is first necessary. The overall process, yielding the μ-1,1 (5C,6C) $\mathbf{P_{prot3}}$ is ∼15 kJ mol^{-1} uphill with two barriers along this rearrangement coordinate, whose heights are estimated to be 23 and 30 kJ mol^{-1} with respect to $\mathbf{P_{prot1}}$ (see the two-dimensional potential-energy surface in Supporting Information, Figure S11B). The alternative, μ-1,2 (6C,6C) hydroperoxo-structure ($\mathbf{P_{prot2}}$) is isoenergetic with $\mathbf{P_{prot3}}$; the pathway to its formation was not found. The structure $\mathbf{P_{prot4}}$ with μ-1,2 (6C,6C) hydroperoxo ligation as in $\mathbf{P_{prot2}}$ but with H^+ on the other oxygen (O_{FeB}) is the least stable among the studied protonated models (27 kJ mol^{-1} above $\mathbf{P_{prot1}}$). We note in passing that the present computational approach does not allow a straightforward linking of the energy scales without and with proton; on the basis of various approximations,[49] we estimate the $\mathbf{P_{prot1}}$-type structure to be ∼35 kJ mol^{-1} above the $\mathbf{P_A}$-type structure.

It is noteworthy that in the case of RNR,[22] a model similar to the present μ-1,2 (6C,6C) hydroperoxo-structure $\mathbf{P_{prot2}}$ was found to be unstable; the O−O bond dissociates spontaneously giving rise to the formation of a Fe^{IV}−OH Fe^{IV}=O product. For Δ^9D, we did not observe such spontaneous homolytic cleavage in $\mathbf{P_{prot2}}$. At the QM(BP/def2-SVP)/MM level, the associated O−O cleavage barrier is predicted to be ∼40 kJ mol^{-1}, and the reaction is exothermic (∼ −60 kJ mol^{-1}). Alternatively,

dx.doi.org/10.1021/ic2018067 | Inorg. Chem. 2012, 51, 2806−2820

Table 4. Calculated Frequencies of Selected Vibrational Modes of Structural Candidates for the P Intermediate[a] for the $M_S = 0$ Antiferromagnetically Coupled Ground State, Using Small in vacuo Cluster Models[b]

class and structure		ν_{O-O} ($\Delta^{18}O$)	$\nu_{s,Fe-O}$ ($\Delta^{18}O$)	$\nu_{as,Fe-O}$ ($\Delta^{18}O$)	$\Delta\nu_{Fe-O}$ ($\Delta^{18}O$)
P	P_A	1076 (−60)	358 (−12)	405 (−20)	47 (−8)
	P_B (2.5 Å)[c]	1074 (−61)	353 (−12)	404 (−20)	51 (−8)
	P_B (3.5 Å)[c]	1066 (−59)	366 (−13)	412 (−22)	46 (−9)
	P_D	1037 (−59)	160 (−55)	406 (−24)	246 (31)
	P_{prot1}	1014 (−57)	368 (−12)	424 (−22)	56 (−10)
P with H^+	P_{prot2}	851 (−42)	324[g] (−25)	418[g] (−23)	94 (+2)
	P_{prot3}	915 (−44)			
	P_{prot4}	886 (−49)	301[g] (−10)	432[g] (−6)	131 (+4)
P with H_2O	P_{w1}	1053 (−59)	358 (−11)	408 (−32)	50 (−21)
	P_{w2} (2.5 Å)[c]	1053 (−59)	354 (−12)	401 (−28)	47 (−16)
	P_{w2} (3.0 Å)[c]	1051 (−60)	359 (−12)	405 (−28)	46 (−16)
	P_{w2} (3.5 Å)[c]	1064 (−61)	367 (−12)	404 (−21)	37 (−9)
	P_{w3}	1145			
	P_{w4}	1181			
	P_{w5}	1092 (−62)	374 (−12)	427 (−22)	53 (−10)
	P_{w6}	1077 (−60)	360 (−9)	440 (−12)	80 (−3)
	P_{w7}	1082 (−61)	388 (−15)	460 (−38)	72 (−23)
	P_{w8}	1087 (−61)	364 (−11)	420 (−16)	56 (−5)
	P_{w9}	1068 (−60)	354 (−12)	401 (−30)	47 (−18)
	P_{w10}	925 (−56)	369 (−12)	411 (−23)	42 (−11)
	P_{w11}	979 (−54)	360 (−13)	428 (−27)	68 (−14)
	P_{w12}	927	441	303	−138
	P_{w13}	955			
P Expt.[d]		898 (−53)	442 (−17)	490 (−19)	48 (−2)
P_{RNR}[e]		976	455		
P_{RNR} Expt.[f]		868 (−47)	457 (−15)	499 (−22)	42 (−7)

[a]In the absence and presence of water molecule and proton. [b]The shifts in vibrational frequencies for the $^{18}O_2$-substituted **P** structures are listed in parentheses ($\Delta^{18}O$). The modes are schematically depicted in Supporting Information, Figure S10. [c]Fe_B-O_{Glu196} distance is restrained. [d]ref 10. [e]Taken from ref 22 but divided by 0.98 to get frequencies comparable with those of Δ^9D which are not multiplied by this empirical scaling factor. [f]Refs 15, 17. [g]Fe−O modes displayed in Supporting Information, Figure S10 become more of Fe_A-O and Fe_B-O character upon binding proton on peroxide ligand.

the QM(B3LYP/def2-TZVP)/MM, QM(M06/TZVP)/MM and QM(M06L/TZVP)/MM calculations predict much higher barriers (~180, ~200, and ~120 kJ mol^{-1}, respectively) and the reaction to be endothermic (~100, ~140, and ~30 kJ mol^{-1}, respectively).

4.5. Spectroscopic Characterization of Protonated Models of the Peroxo Intermediate. *Electronic Spectroscopy.* As mentioned above, we consider the protonated models as possible candidates for **P** and the putative **P′** intermediate in Δ^9D. Because a **P′** intermediate has not been observed in Δ^9D, spectral properties can only be compared to experimental results for **P** in Δ^9D and **P′** in RNR. Considering first the calculated *J*-coupling constants, we found that all are negative (see Table 2) confirming the antiferromagnetic interaction in the electronic ground state, which is in line with measurements on **P** Δ^9D and **P′** in RNR. We furthermore note that structures with protonated peroxide exhibit much less negative values (from −20 to −30 cm^{-1}) than structures with H^+ at the terminal Glu105 (~ −90 cm^{-1}).

Experimental studies on absorption spectra show that the characteristic broad LMCT band of the **P′** RNR intermediate is much weaker and blue-shifted (ε_{max} ~ 200 M^{-1} cm^{-1} at 20000 cm^{-1})[20] compared to **P** intermediates in both RNR and Δ^9D (see Table 1). In Figure 6, the calculated absorption spectra of protonated models of the peroxo intermediate $\mathbf{P_{prot1}}$ and $\mathbf{P_{prot3}}$ (and $\mathbf{P_A}$ for comparison) are displayed. Both the $\mathbf{P_{prot1}}$ and $\mathbf{P_{prot3}}$ models exhibit $\pi^*_{peroxide} \rightarrow Fe^{III}$ CT transitions spread over the range of 6000−23000 cm^{-1}, which form a double-hill absorption profile with the intensity weaker than the CT bands of $\mathbf{P_A}$ (~600 instead of ~1200 M^{-1} cm^{-1}). This result is in line with significantly decreased LMCT intensity in experiments in going from **P** RNR to **P′** RNR (~1200 to 200 M^{-1} cm^{-1}). On the other hand, the experimentally observed blue-shift of the most intense $\pi^*_{peroxide} \rightarrow Fe^{III}$ LMCT band is not apparent if we compare the calculations for $\mathbf{P_{prot1}}$ and $\mathbf{P_{prot3}}$ with those for $\mathbf{P_A}$.

Concerning the higher-energy isomers $\mathbf{P_{prot2}}$ and $\mathbf{P_{prot4}}$, we find the opposite situation (spectra are provided in Supporting Information, Figure S13). They have a broad CT band located between 15000 and 25000 cm^{-1}, therefore clearly shifted to higher energies, but with intensity comparable to the most intense $\pi^*_{peroxide} \rightarrow Fe^{III}$ transition in $\mathbf{P_A}$.

All these observations suggest that none of the studied protonated peroxo intermediate models conform to the spectroscopic characterization of **P** Δ^9D. Alternatively, they could be candidates for **P′** Δ^9D. The agreement of the calculated spectral features with experiment for **P′** RNR is modest.

Mössbauer Isomer Shifts. The agreement between experimental Mössbauer shifts for **P** Δ^9D (0.64/0.68 mm s^{-1}) and the values calculated for the protonated QM/MM models (see Table 3) is less satisfactory than that in the absence of proton; although within the error bars of the computations, only $\mathbf{P_{prot3}}$ can be rigorously excluded. For the energetically most favored $\mathbf{P_{prot1}}$ structure (with protonated Glu105 forming a hydrogen bond with peroxide bridge), the isomer shifts are calculated to be 0.57/0.60 mm s^{-1} which is consistent with the computational results for a similar structure in ref 22.

dx.doi.org/10.1021/ic2018067 | Inorg. Chem. 2012, 51, 2806−2820

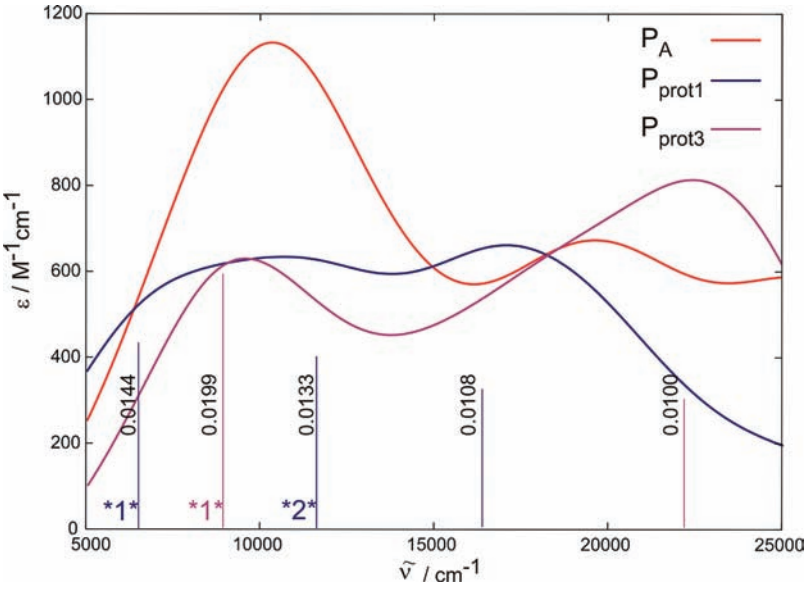

Figure 6. Calculated electronic absorption spectrum of $\mathbf{P}_{prot1}$ and $\mathbf{P}_{prot3}$ (for the sake of comparison the spectrum of the $\mathbf{P}_A$ structure is also displayed). Spectra were calculated for $M_S = 0$ with TD-DFT(B3LYP)/def2-TZVP + point-charges at the QM/MM equilibrium geometry. Bands were modeled using hybrid Gaussian/Lorentzian line shape (both with relative weight of 0.5) with arbitrarily chosen bandwidth (fwhm) of 7000 cm^{-1} (Abs). Values of the largest oscillator strengths ($f \geq 0.01$) are provided as numbers next to the corresponding peaks. The Kohn–Sham orbitals involved in the most characteristic transitions are depicted in Supporting Information, Figure S12.

Notably, for the μ-1,1 $\mathbf{P}_{prot3}$ structure we calculate $\delta_{FeA/FeB}$ = 0.47/0.62 mm s^{-1}, which closely match the experimental isomer shifts of **P′** in RNR (0.45/0.60 mm s^{-1}).[20] Moreover, the difference in the quadrupole splitting between two iron centers behaves similarly in the calculations when going from $\mathbf{P}_A$ (or $\mathbf{P}_B$) to $\mathbf{P}_{prot3}$ as observed experimentally in going from **P** Δ^9D to **P′** RNR ($|\Delta\Delta E_Q|$ using Approach 2: $\mathbf{P}_A$ 0.41 mm s^{-1} and $\mathbf{P}_{prot3}$ 0.57 mm s^{-1} vs experimental **P** Δ^9D 0.84 mm s^{-1} and **P′** RNR 0.98 mm s^{-1}). Combined with the energetic accessibility of the $\mathbf{P}_{prot3}$, this structure may be considered as a plausible structural model for a putative **P′** intermediate in Δ^9D.

Vibrational Spectroscopy. The values of the calculated O–O and the two Fe–O stretching frequencies for all protonated structures are summarized in Table 4. In comparison with the frequencies of nonprotonated μ-1,2 structures ($\mathbf{P}_A$, $\mathbf{P}_B$), the O–O stretching mode in the μ-1,2 or μ-1,1 structures with protonated peroxide moiety ($\mathbf{P}_{prot2}$; $\mathbf{P}_{prot3}$; $\mathbf{P}_{prot4}$) is shifted by 150–200 cm^{-1} to lower wavenumbers, whereas for μ-1,2 $\mathbf{P}_{prot1}$ with H^+ on Glu105, this mode is weakened by only about 50 cm^{-1}. Additionally, in contrast to nonprotonated models, the Fe–O modes in the μ-1,2 peroxo models with H^+ located on the peroxide are more localized and have an increased Fe_A-O and Fe_B-O character. The mode having the larger Fe–OH contribution is shifted to lower wavenumbers by about 40–70 cm^{-1} compared to the symmetric mode in the nonprotonated μ-1,2 peroxo models. On the basis of the comparison with experimental data on **P** Δ^9D vibrations, we can safely exclude $\mathbf{P}_{prot2}$, $\mathbf{P}_{prot3}$, and $\mathbf{P}_{prot4}$ as **P** Δ^9D models. The agreement is not poor for $\mathbf{P}_{prot1}$, but even that structure is less successful than the nonprotonated models in reproducing $\Delta\nu_{Fe-O}$ and the isotopic shifts.

Summarizing the results presented above, it appears that there is no protonated peroxodiferric structure among the candidates studied whose spectroscopic parameters correlate satisfactorily with those of **P** Δ^9D. On the other hand, three candidates, $\mathbf{P}_{prot1}$, $\mathbf{P}_{prot2}$, and $\mathbf{P}_{prot3}$, could be relevant as a putative **P′** Δ^9D intermediate.

4.6. Geometric and Energetic Characterization of Hydrated Models of the Peroxo Intermediate. The crystal structure of the reduced Δ^9D contains a water molecule at a distance of 2.8 Å from one of the irons (see Supporting Information, Figure S5). This suggests that the water molecule may be an integral part of the peroxo intermediate or the coordination may play a role in its activation. Twelve corresponding structural models were therefore subjected to the QM/MM optimization (denoted by **P** + $H_2O \equiv \mathbf{P}_{wn}$, Figure 7), differing in the position of the added water molecule and the peroxide coordination. The water molecule can be bound by hydrogen bonds to μ-1,2 peroxides ($\mathbf{P}_{w1}$, $\mathbf{P}_{w2}$), or occupy "axial" coordination position on the iron centers, leading to a monodentate peroxide ($\mathbf{P}_{w3}$, $\mathbf{P}_{w4}$). There are also several possibilities for water coordination to the irons in the equatorial plane, associated with opening of a bridging carboxylate but leaving the μ-1,2 peroxide intact ($\mathbf{P}_{w5}$–$\mathbf{P}_{w9}$). Finally, water dissociation and subsequent coordination of H^+ and OH^- ($\mathbf{P}_{w10}$, $\mathbf{P}_{w11}$), as well as water binding to η^2 peroxide complexes can be envisaged ($\mathbf{P}_{w12}$, $\mathbf{P}_{w13}$).

Among the isomers studied, the most stable structure at the QM/MM level corresponds to the (6C,6C) μ-1,2-peroxodiferric complex (see Figure 7 and Table 2) in which the water molecule interacts with the peroxide ligand via a hydrogen bond (denoted as $\mathbf{P}_{w1}$ and closely resembling $\mathbf{P}_A$). In a close analogy to **P** structures in the absence of a water molecule, the (6C,5C) $\mathbf{P}_{w2}$ structure with Glu196 bound to the Fe_B ion in a monodentate fashion is only slightly higher in energy than the reference $\mathbf{P}_{w1}$. However, analogously to $\mathbf{P}_B$, $\mathbf{P}_{w2}$ is not a local minimum on the respective QM/MM potential energy surface (PES). When the Fe_B-O_{Glu196} distance was restrained to 2.5, 3.0, and 3.5 Å, the QM/MM calculations yielded energies that were 2, 3, and 8 kJ mol^{-1} higher than the most stable isomer $\mathbf{P}_{w1}$, respectively. These energies again indicate a high degree of flexibility of Glu196 with respect to its distortion from bidentate to monodentate coordination mode.

dx.doi.org/10.1021/ic2018067 | *Inorg. Chem.* 2012, 51, 2806–2820

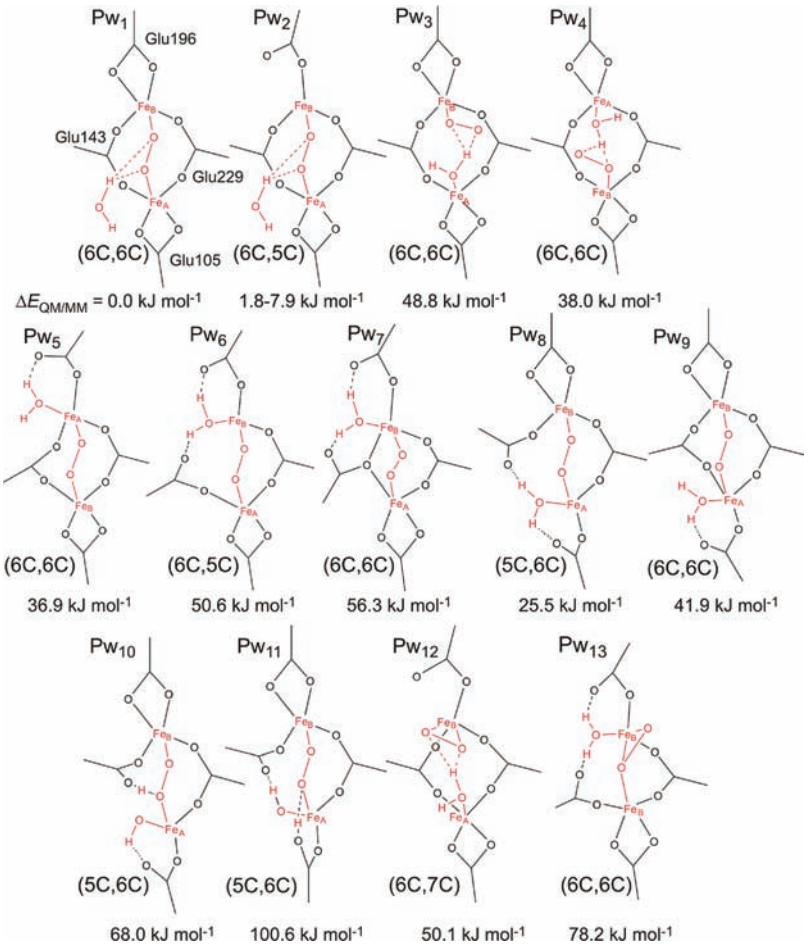

Figure 7. QM/MM structural models of the Δ^9D **P** intermediate with a water molecule in the active site, together with their computed relative energies. The figure shows a top view, with the irons, peroxide, water, and the Glu residues in the equatorial positions. His residues that are below the plane, and the substrate above the plane is not displayed (cf. Figure 1). For the sake of clarity, the representation is only schematic (e.g., the additional hydrogen-bond acceptors of water molecules in $\mathbf{P_{w1}}$ and $\mathbf{P_{w2}}$ coming from the MM system (Tyr111) are not depicted).

Considering further the possibilities with a μ-1,2 peroxide structure, one can notice that if only the $\Delta E_{\text{QM-vac}}$ values are considered (QM energies for the QM/MM geometries; that is, ignoring the effect of the protein environment on the QM/MM energy), the μ-1,2 structures with a water molecule bound to irons in the equatorial plane (i.e., $\mathbf{P_{w5}}$, $\mathbf{P_{w6}}$, $\mathbf{P_{w7}}$, $\mathbf{P_{w8}}$, $\mathbf{P_{w9}}$) are energetically comparable with or even more stable than $\mathbf{P_{w1}}$. A similar finding was made for the cluster model of RNR that included the second-shell residues,[22] suggesting the inherent thermodynamic stability of this type of water adduct in vacuo. However, the electrostatic interactions of the active site with the array of point charges representing the protein electrostatic field destabilize these QM/MM structures compared to the reference $\mathbf{P_{w1}}$. Thus, all these structures are energetically less stable than $\mathbf{P_{w1}}$ in QM/MM calculations (~25−70 kJ mol^{-1}). We were not able to unambiguously identify the amino acids responsible for this significant electrostatic destabilization in the QM/MM calculations.

It is apparent that alternative peroxide coordination modes are also disfavored: the end-on η^1-type $\mathbf{P_{w3}}$ and $\mathbf{P_{w4}}$ isomers, the side-on η^2 $\mathbf{P_{w12}}$ isomer, and the side-on μ-η^2:η^1 $\mathbf{P_{w13}}$ are all higher in energy than $\mathbf{P_{w1}}$ by 38−78 kJ mol^{-1}. Among these, only for $\mathbf{P_{w13}}$ originates a significant contribution to the destabilization from electrostatic interactions of the QM active site with the MM protein environment ($\Delta E_{\text{QM-vac}}$ = 12 kJ mol^{-1} vs $\Delta E_{\text{QM/MM}}$ = 78 kJ mol^{-1}). Finally, the $\mathbf{P_{w10}}$ and $\mathbf{P_{w11}}$ structures obtained by allowing the dissociation of the coordinated water into OH^- and H^+ were also found to be unstable (42 and 101 kJ mol^{-1}); in the case of $\mathbf{P_{w10}}$, this stems from the environment ($\Delta E_{\text{QM-vac}}$ = −15 kJ mol^{-1}). This is in line with a similar finding made in the RNR **P** intermediate study[22] in which μ-1,2 (OH^-,H^+) structures were found to be less stable by 20−70 kJ mol^{-1} compared to the μ-1,2 ($+H_2O$) structures.

4.7. Spectroscopic Characterization of Hydrated Models of the Peroxo Intermediate. *Electronic Spectroscopy.* All the QM/MM structures have negative *J*-coupling constants (mostly ranging from −80 to −120 cm^{-1}; see Table 2), which are in line with the expected value for the **P** Δ^9D intermediate. The only exception is the side-on η^2 $\mathbf{P_{w12}}$ model having positive *J* value (40 cm^{-1}).

The calculated TD-DFT absorption and CD spectra of all structures are depicted in Supporting Information, Figures S14 and S15. According to these data, the peroxide → Fe^{III} CT band located between ~10000 and ~12500 cm^{-1} is characteristic for all of the $\mathbf{P_w}$ models. These structures furthermore exhibit another LMCT band in the 18000−25000 cm^{-1} region, which is also a result of transitions with a peroxide → Fe^{III} character. The spectra of $\mathbf{P_{w1}}$/$\mathbf{P_{w2}}$ were found to fit the experimental data on **P** best; as they are very similar to those of

dx.doi.org/10.1021/ic2018067 | Inorg. Chem. 2012, 51, 2806−2820

the related $\mathbf{P_A}/\mathbf{P_B}$, their detailed discussion is presented in the Supporting Information.

Mössbauer Isomer Shifts. The computed isomer shifts of all hydrated **P** structures are collected in Table 3. The most stable structure $\mathbf{P_{w1}}$ possesses shifts of 0.67 and 0.68 mm s^{-1}, which are somewhat too symmetric in comparison with the experimental values for Δ^9D **P** (0.64/0.68 mm s^{-1}). Elongating the distance between Fe_B-O_{Glu196} in $\mathbf{P_{w1}}$, that is, forming $\mathbf{P_{w2}}$, the isomer shifts of two irons become more inequivalent. For a distance of 2.5 Å, the calculated values are 0.67 and 0.64 mm s^{-1}, which are close to the experimental δ's of **P** in Δ^9D, and consistent with those calculated for $\mathbf{P_B}$. As can be seen in Table 3, the other structural models do not agree with the experimental values for the **P** intermediate. A very similar conclusion can be drawn in general from Supporting Information, Table S4 containg δ and ΔE_Q values calculated with Approach 2; but there is a noticeable difference for the $\mathbf{P_{w8}}$ model. Unlike Approach 1 (Table 3), Approach 2 predicts 0.66/0.70 mm s^{-1}, in accordance with experimental data on **P** in Δ^9D.

Concerning a putative **P′** intermediate in Δ^9D, only the values 0.53/0.65 mm s^{-1} calculated using Approach 1 for the $\mathbf{P_{w8}}$ structure (with equatorial H_2O coordination to Fe_A and opened carboxylate bridge) resemble the experimental 0.45/0.60 mm s^{-1} determined for RNR **P′**. Considering its energetic accessibility, this H_2O coordinated structure may be relevant as a **P′** structure along the reaction coordinate of Δ^9D.

Vibrational Spectroscopy. According to Table 4, the experimental[10] $\Delta\nu_{Fe-O}$ value (48 cm^{-1}) agrees well with calculated $\Delta\nu_{Fe-O}$ values for both $\mathbf{P_{w1}}$ and $\mathbf{P_{w2}}$ with Fe_B-O_{Glu196} of 2.5 Å (50 and 47 cm^{-1}). The agreement between the calculated and experimental value of the isotopic shifts, $\Delta\nu_{Fe-O}$ (Δ^{18}O), is worse (e.g., −21 cm^{-1} for the $\mathbf{P_{w1}}$ vs −2 cm^{-1} for the Δ^9D **P**). For most structures with a μ-1,2 O_2^{2-}-binding mode and H_2O bound in equatorial positions and an open carboxylate ($\mathbf{P_{w5}}$, $\mathbf{P_{w8}}$, $\mathbf{P_{w9}}$, $\mathbf{P_{w10}}$, and $\mathbf{P_{w11}}$), the difference of $\Delta\nu_{Fe-O}$ from the experimental values is only 5−8 cm^{-1}; for $\mathbf{P_{w8}}$, even the isotopic shift is close to the experiment (for $\mathbf{P_{w6}}$ and $\mathbf{P_{w7}}$, the error in $\Delta\nu_{Fe-O}$ is greater than 20 cm^{-1}). Although the calculated vibrational frequencies for these structures are in reasonable agreement with experimental data, neither their energetic nor their Mössbauer δ characteristics are consistent with experiment.

The η^1-type isomers, $\mathbf{P_{w3}}$ and $\mathbf{P_{w4}}$, have about 50−100 cm^{-1} higher O−O stretching frequencies than the μ-1,2 structures and lack the pattern of two low-lying frequencies associated with the antisymmetric and symmetric Fe−O vibrational modes. Also, η^2 $\mathbf{P_{w12}}$ and μ^2-η^2:η^1 $\mathbf{P_{w13}}$ disagree with the experimental (rR) data for the Δ^9D **P** intermediate.

We may conclude that from an energetic and spectroscopic point of view, the best **P** Δ^9D candidates among the studied structural models in the presence of a water molecule are $\mathbf{P_{w1}}$ and $\mathbf{P_{w2}}$ (with Fe_B-$O_{Glu196} \leq 3$ Å) whereas the structures with η^1, η^2 or μ-η^2:η^1 O_2^{2-}-ligation are not satisfactory based on either spectroscopic or energetic requirements. Furthermore, it seems that the dissociation of bound H_2O to OH^- and H^+ in the coordination sphere of metal centers leads to structures that are at high energy with respect to $\mathbf{P_{w1}}$ which excludes them as the potential candidates for the Δ^9D **P** and possibly **P′**. Finally, μ-1,2 $\mathbf{P_{w8}}$ (with H_2O bound to Fe_A in the equatorial plane and open bridging carboxylate) is the best candidate in this group for the supposed **P′** in Δ^9D since it is energetically feasible.

4.8. Activation of P Intermediate in Δ^9D. In the previous sections, we made efforts to assign the structure of the experimentally observed Δ^9D **P** based on energetic and spectroscopic data. As mentioned in the introduction, the motivation for searching for an activated **P′** Δ^9D intermediate is 2-fold. First, there exist analogous nonheme diiron enzymes, particularly RNR and ToMO, where such an intermediate has been experimentally characterized. Second, in vitro prepared **P** Δ^9D is not reactive toward hydrogen abstraction from the substrate, which might be the result of some missing activation step.

In the present study, no detailed QM/MM calculations were carried out concerning the feasibility of the hydrogen abstraction step. However, on the basis of energetic accessibility, and spectroscopic properties being similar to **P′** in RNR, we first suggest as a plausible **P′** intermediate in Δ^9D the μ-1,2 (5C,6C) structure ($\mathbf{P_{prot1}}$) with a protonated terminal Glu105 ligand (the proton coming either from His203 or solvent, see section 4.4), whose energy is estimated to be ∼35 kJ mol^{-1} higher than the reference $\mathbf{P_A}$.[49] Interestingly, $\mathbf{P_{prot1}}$ converts easily to a μ-1,1 structure ($\mathbf{P_{prot3}}$) with a protonated peroxide moiety (only ∼15 kJ mol^{-1} above $\mathbf{P_{prot1}}$ and separated by barrier of ∼30 kJ mol^{-1}); the alternative $\mathbf{P_{prot2}}$ structure with protonated μ-1,2 peroxide seems also energetically accessible. Such hydroperoxide-$Fe^{III}Fe^{III}$ forms are appealing because of their possible reactivity toward C−H bond cleavage as it was determined for a similar HOO-Fe^{III} moiety in activated bleomycin.[51] This description (depicted in Scheme 1, left-hand side) would be different from that developed in ref 22 for RNR chemistry, where proton transfer in going from **P** to **P′** would activate the diferric site for one-electron reduction to give the spectroscopically well-characterized μ-oxo Fe(III)Fe(IV) **X** intermediate responsible for a homolytic O−H bond cleavage from Tyr.

The alternative possibility for a **P′** in Δ^9D would be the H_2O-bound μ-1,2 (6C,6C) structure ($\mathbf{P_{w8}}$) lying only ∼25 kJ mol^{-1} above the reference $\mathbf{P_{w1}}$ structure. Preliminary QM/MM and QM-only results indicate that it is not capable of cleaving the C−H bond, but the bound H_2O in $\mathbf{P_{w8}}$ can dissociate to give rise to $\mathbf{P_{w10}}$ (42 kJ mol^{-1} above $\mathbf{P_{w8}}$). The $\mathbf{P_{w10}}$ structure has a proton on Glu143 forming a hydrogen bond with the peroxide ligand. This would allow a proton transfer resulting in the formation of a structure similar to $\mathbf{P_{prot3}}$ but with the hydroxide in the coordination sphere (denoted as $\mathbf{P_{w10}}$*); the hydrogen abstraction could then proceed as described above (see Scheme 1, right-hand side).

The role of protonation in the active center is the subject of intensive research also in other related nonheme diiron enzymes. For MMO, experiments show that proton uptake is involved in the interconversion of the two suggested peroxo intermediates and also in their further transformation via O−O cleavage to a diiron(IV) species.[3] On the basis of studies on a model complex,[52] the first protonation was proposed to involve the bridging carboxylate, thereafter becoming monodentate. Related computational studies,[53,54] on the other hand, show no involvement of protons in the rate determining step, ascribing their effect to alterations in the structure of the enzyme or in its complexation with the regulatory protein.

ToMO and T4MO, on the other hand, possess some features that resemble the Δ^9D. For those enzymes, no O−O cleavage to diiron(IV) species seems to be involved in the catalysis;[4] the hydroxylation is brought about by a peroxo species that has spectroscopic properties more similar to RNR **P′** than to **P**-type intermediates.[21] Experiments with T201 variants of ToMO suggest that this amino acid plays a critical role in a proton transfer step, necessary to generate the peroxo intermediate.[55]

dx.doi.org/10.1021/ic2018067 | *Inorg. Chem.* 2012, 51, 2806−2820

Scheme 1. Suggested Proton and Water Mechanism of O_2 Activation in Δ^9D

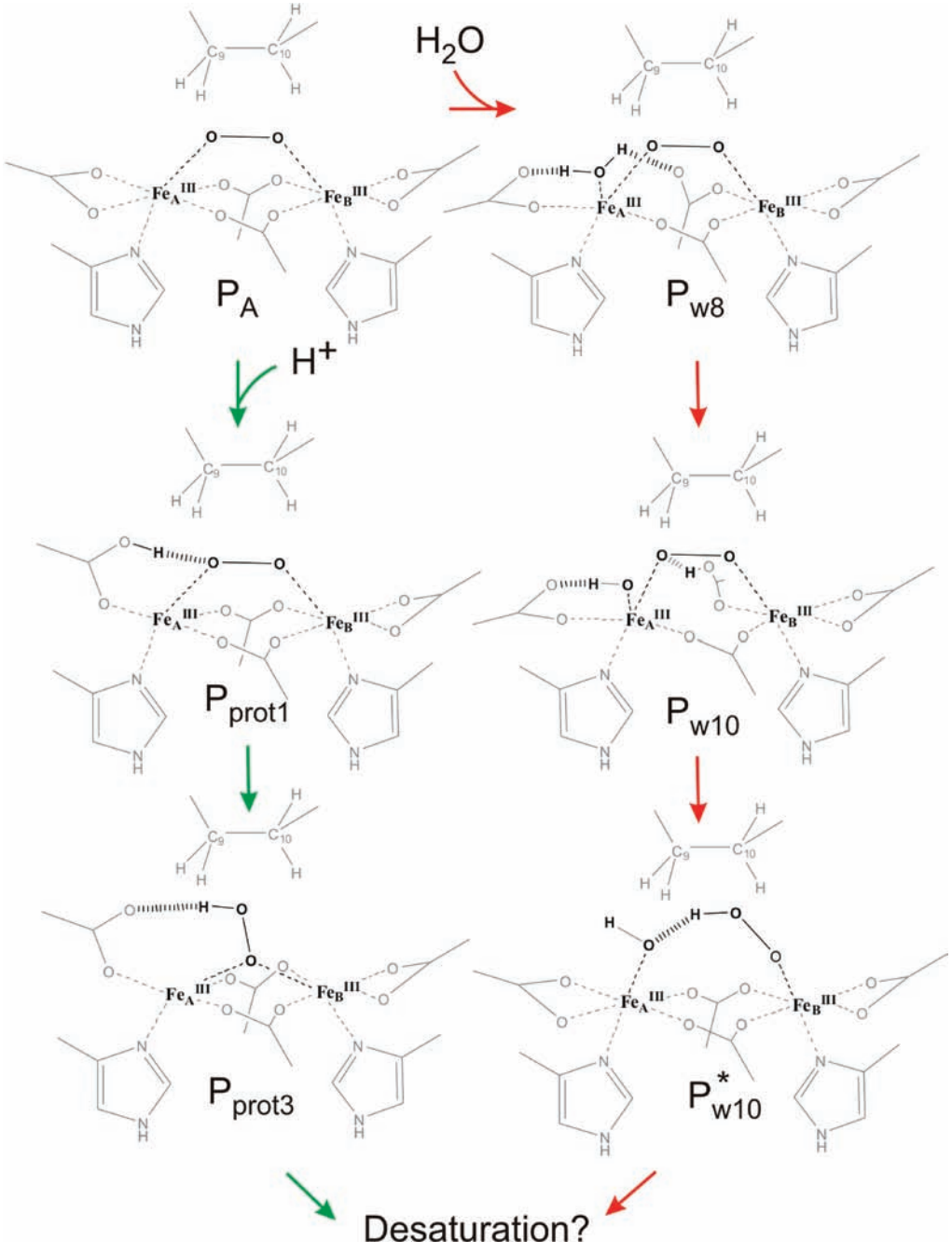

A recent theoretical study,[56] providing a plausible explanation for the different pathways in ToMO/T4MO and MMO based on a hydrogen-bond chain toward the peroxo moiety, furthermore suggests that the only way to reconcile theoretical spectroscopic data for this peroxo intermediate with experiments is to assume a protonated peroxo ligand. Such a species would be analogous to the Δ^9D $\mathbf{P}_{prot3}$ or $\mathbf{P}_{w10}$* (see Scheme 1), considered here as possible intermediates on the pathway toward desaturation.

5. CONCLUSIONS

To reveal the best structural candidates for the **P** and putative **P′** intermediates in Δ^9D we have investigated three sets of peroxodiferric structures (differing in the absence or presence of a H^+ and a H_2O in the active site) and correlated QM/MM energetic and spectroscopic results with the experimental data. The QM(DFT)/MM methodology used has been validated in several studies[57−59] to provide reasonable energetics and mechanistic insight for many complex enzymatic reactions.

First, we have demonstrated that the effect of substrate binding on coordination and CD spectroscopic properties in reduced Δ^9D can be qualitatively reproduced in calculations, and it is corroborated to involve transition of one of the irons from a five to a four coordinate structure. This also confirmed that our methods can reasonably correlate structural and spectroscopic data.

Second, we have clearly shown that structural models whose spectroscopic (i.e., absorption, CD, vibrational, and Mössbauer) characteristics correlate best with experimental data for the Δ^9D

dx.doi.org/10.1021/ic2018067 | Inorg. Chem. 2012, 51, 2806−2820

P intermediate feature a μ-1,2-O_2^{2-} binding mode, regardless of the absence or presence of an additional proton or water molecule in the active site. The best candidates reproduce experimental results within the error bars of the quantum chemical methods utilized. Interestingly, restraining the Fe_B-O_{Glu196} bond to ~2.5 Å (monodentate carboxylate, five-coordinate iron) in most cases gives better agreement with the spectroscopic (particularly Mössbauer) data than for the optimized structure (bidentate carboxylate, six-coordinate iron). The small energy difference between these geometries suggests significant flexibility of this ligand, which might explain the absence of the five-coordinate local minimum in our calculations.

Third, on the basis of the energetic accessibility of the corresponding structures, we have suggested that protonation of the peroxide moiety, possibly with preceding water binding, could be responsible for the conversion of the **P** intermediate in Δ^9D into a form capable of hydrogen abstraction; this reaction step remains to be explored.

In summary, a combination of QM/MM calculations using calibrated methods and experimental data allowed us to formulate a consistent picture for the initial stages of the reaction catalyzed by Δ^9D, an important diferrous nonheme iron enzyme that cleaves the C−H bonds in alkane chains resulting in the highly specific insertion of double bonds. The present study provides the basis for the investigation of the mechanism of desaturation by Δ^9D, which is now underway.

■ ASSOCIATED CONTENT

Supporting Information

Further details are given as noted in the text and in Figure S1−S16 and Tables S1−S4. This material is available free of charge via the Internet at http://pubs.acs.org.

■ AUTHOR INFORMATION

Corresponding Author

*E-mail: edward.solomon@stanford.edu (E.I.S.), rulisek@uochb.cas.cz (L.R.).

Notes

The authors declare no competing financial interest.

■ ACKNOWLEDGMENTS

We thank Prof. Brian Fox, University of Wisconsin, Madison, for the enzyme samples used for the spectroscopy and for insightful discussions. The project was supported by the Ministry of Education, Youth, and Sports of the Czech Republic (Projects Z40550506 and LC512). E.I.S. thanks NSF MCB (0919027) for support of these studies at Stanford.

■ REFERENCES

(1) Lindqvist, Y. In *Handbook of Metalloproteins*; Messerschmidt, A., Huber, R., Wieghardt, K., Poulos, T.; Eds.; Wiley: New York, 2001; pp 725−737.

(2) Solomon, E. I.; Brunold, T. C.; Davis, M. I.; Kemsley, J. N.; Lee, S.-K.; Lehnert, N.; Neese, F.; Skulan, A. J.; Yang, Y.-S.; Zhou, J. *Chem. Rev.* **2000**, *100*, 235−349.

(3) Tinberg, C. E.; Lippard, S. J. *Acc. Chem. Res.* **2011**, *44*, 280−288.

(4) Murray, L. J.; Lippard, S. J. *Acc. Chem. Res.* **2007**, *40*, 466−474.

(5) Fox, B. G.; Lyle, K. S.; Rogge, C. E. *Acc. Chem. Res.* **2004**, *37*, 421−429.

(6) Yang, Y.-S.; Broadwater, J. A.; Pulver, S. C.; Fox, B. G.; Solomon, E. I. *J. Am. Chem. Soc.* **1999**, *121*, 2770−2783.

(7) Song, W. J.; Behan, R. K.; Naik, S. G.; Huynh, B. H.; Lippard, S. J. *J. Am. Chem. Soc.* **2009**, *131*, 6074−6075.

(8) Song, W. J.; Lippard, S. J. *Biochemistry* **2011**, *50*, 5391−5399.

(9) Reipa, V.; Shanklin, J. *Chem. Commun.* **2004**, 2406−2407.

(10) Broadwater, J. A.; Ai, J.; Loehr, T. M.; Sanders-Loehr, J.; Fox, B. G. *Biochemistry* **1998**, *37*, 14664−14671.

(11) Broadwater, J. A.; Achim, C.; Münck, E.; Fox, B. G. *Biochemistry* **1999**, *38*, 12197−12204.

(12) Sobrado, P.; Lyle, K. S.; Kaul, S. P.; Turco, M. M.; Arabshahi, I.; Marwah, A.; Fox, B. G. *Biochemistry* **2006**, *45*, 4848−4858.

(13) Krebs, C.; Bollinger, J. M. Jr.; Theil, E. C.; Huynh, B. H. *J. Biol. Inorg. Chem.* **2002**, *7*, 863−869.

(14) Bollinger, J. M.; Krebs, C.; Vicol, A.; Chen, S. X.; Ley, B. A.; Edmondson, D. E.; Huynh, B. H. *J. Am. Chem. Soc.* **1998**, *120*, 1094−1095.

(15) Skulan, A. J.; Brunold, T. C.; Baldwin, J.; Saleh, L.; Bollinger, J. M. Jr.; Solomon, E. I. *J. Am. Chem. Soc.* **2004**, *126*, 8842−8855.

(16) Lyle, K. S.; Haas, J. A.; Fox, B. G. *Biochemistry* **2003**, *42*, 5857−5866.

(17) Moenne-Loccoz, P.; Baldwin, J.; Ley, B.; Loehr, T.; Bollinger, J. *Biochemistry* **1998**, *37*, 14659−14663.

(18) Baldwin, J.; Voegtli, W.; Khidekel, N.; Moenne-Loccoz, P.; Krebs, C.; Pereira, A.; Ley, B.; Huynh, B.; Loehr, T.; Riggs-Gelasco, P.; Rosenzweig, A.; Bollinger, J. *J. Am. Chem. Soc.* **2001**, *123*, 7017−7030.

(19) Yun, D.; Garcia-Serres, R.; Chicalese, B. M.; Na, Y. H.; Huynh, B. H.; Bollinger, J. M. Jr. *Biochemistry* **2007**, *46*, 1925−1932.

(20) Saleh, L.; Krebs, C.; Ley, B. A.; Naik, S.; Huynh, B. H.; Bollinger, J. M. Jr. *Biochemistry* **2004**, *43*, 5953−5964.

(21) Murray, L. J.; Naik, S. G.; Ortillo, D. O.; Garcia-Serres, R.; Lee, J. K.; Huynh, B. H.; Lippard, S. J. *J. Am. Chem. Soc.* **2007**, *129*, 14500−14510.

(22) Jensen, K. P.; Bell, C. B.; Clay, M. D.; Solomon, E. I. *J. Am. Chem. Soc.* **2009**, *131*, 12155−12171.

(23) Ryde, U. *J. Comput.-Aided Mol. Design* **1996**, *10*, 153−164.

(24) Ryde, U.; Olsson, M. H. M. *Int. J. Quantum Chem.* **2001**, *81*, 335−347.

(25) Treutler, O.; Ahlrichs, R. *J. Chem. Phys.* **1995**, *102*, 346−354.

(26) Case, D. A.; Pearlman, D. A.; Caldwell, J. W.; Cheatham, III, T. E.; Wang, J.; Ross, W. S.; Simmerling, C. L.; Darden, T. A.; Merz, K. M.; Stanton, R. V.; Cheng, A. L.; Vincent, J. J.; Crowley, M.; Tsui, V.; Gohlke, H.; Radmer, R. J.; Duan, Y.; Pitera, J.; Massova, I.; Seibel, G. L.; Singh, U. C.; Werner, P. K.; Kolman, P. A. *AMBER 7*; University of California: San Francisco, CA, 2002.

(27) Cornell, W. D.; Cieplak, P.; Bayly, C. I.; Gould, I. R.; Merz, K. M.; Ferguson, D. M.; Spellmeyer, D. C.; Fox, T.; Caldwell, J. W.; Kolman, P. A. *J. Am. Chem. Soc.* **1995**, *117*, 5179−5197.

(28) Svensson, M.; Humbel, S.; Froese, R. D. J.; Matsubara, T.; Sieber, S.; Morokuma, K. *J. Phys. Chem.* **1996**, *100*, 19357−19363.

(29) Reuter, N. I.; Dejaegere, A.; Maigret, B.; Karplus, M. *J. Phys. Chem.* **2000**, *104*, 1720−1735.

(30) Lindqvist, Y.; Huang, W. J.; Schneider, G.; Shanklin, J. *EMBO J.* **1996**, *15*, 4081−4092.

(31) Sigfridsson, E.; Ryde, U. *J. Comput. Chem.* **1998**, *19*, 377−395.

(32) Neese, F. *ORCA, An ab initio, Density Functional, and Semiempirical Program Package*; University of Bonn: Bonn, Germany, 2007.

(33) Becke, A. D. *Phys. Rev. A* **1988**, *38*, 3098−3100.

(34) Perdew, J. P. *Phys. Rev. B* **1986**, *33*, 8822−8824.

(35) Vosko, S. H.; Wilk, L.; Nusair, M. *Can. J. Phys.* **1980**, *58*, 1200−1211.

(36) Weigend, F.; Ahlrichs, R. *Phys. Chem. Chem. Phys.* **2005**, *7*, 3297−3305.

(37) Eichkorn, K.; Treutler, O.; Öhm, H.; Häser, M.; Ahlrichs, R. *Chem. Phys. Lett.* **1995**, *240*, 283−290.

(38) Eichkorn, K.; Weigen, F.; Treutler, O.; Ahlrichs, R. *Theor. Chim. Acta* **1997**, *97*, 119−124.

(39) Lee, C. T.; Yang, W. T.; Parr, R. G. *Phys. Rev. B* **1988**, *37*, 785−789.

(40) Becke, A. D. *J. Chem. Phys.* **1993**, *98*, 5648−5652.

(41) The final electronic spectra were obtained as a sum of Gaussian/Lorentzian functions centered at the wavenumbers of the corresponding

electronic transitions according to the equations introduced in Supporting Information as Equation 1 (absorption spectrum) and Equation 2 (CD spectrum).
(42) Neese, F. *Inorg. Chim. Acta* **2002**, *337*, 181−192.
(43) Schäfer, A.; Horn, H.; Ahlrichs, R. *J. Chem. Phys.* **1992**, *97*, 2571−2577.
(44) Noodleman, L. *J. Chem. Phys.* **1981**, *74*, 5737−5743.
(45) Yamaguchi, K.; Takahara, Y.; Fueno, T. In *Applied Quantum Chemistry*; Smith, V. H., Ed.; Reidel: Dordrecht, The Netherlands, 1986; p 155.
(46) Vancoillie, S.; Zhao, H.; Radoń, M.; Pierloot, K. *J. Chem. Theory Comput.* **2010**, *6*, 576−582.
(47) Grimme, S.; Neese, F. *J. Chem. Phys.* **2007**, *127*, 154116.
(48) Besley, N. A.; Robinson, D. *Faraday Discuss.* **2011**, *148*, 55−70.
(49) To obtain a very qualitative estimate of the (free) energy change involved in the process of protonating $\mathbf{P_A}$ to obtain $\mathbf{P_{prot1}}$, we carried out calculations for a proton transfer from the water solvent represented by a hybrid model (the cluster $[H_3O(H_2O)_2]^+$ solvated in a water continuum using COSMO[50]) to a first-shell $\mathbf{P_A}$-like cluster model, which results in the formation of a $\mathbf{P_{prot1}}$-like structure. This process was found to be endergonic by $\Delta G \approx 34$ kJ mol^{-1}. Alternatively, in cluster calculations including second shell residues (described in the Supporting Information), we considered a $\mathbf{P_{prot1}}$-like isomer (c-$\mathbf{P_F}$) using His203 as the proton source, thereby allowing direct comparison with a $\mathbf{P_A}$-like isomer (c-$\mathbf{P_A}$). The computed energy demand of protonation is 35.4 kJ mol^{-1} in this case.
(50) COSMO stands for COnductor-like Screening MOdel. See: Klamt, A.; Schuurmann, G. *J. Chem. Soc., Perkin Trans. 2* **1993**, 799−805.
(51) Neese, F.; Zaleski, J. M.; Zaleski, K. L.; Solomon, E. I. *J. Am. Chem. Soc.* **2000**, *122*, 11703−11724.
(52) Do, L. H.; Hayashi, T.; Moënne-Loccoz, P.; Lippard, S. J. *J. Am. Chem. Soc.* **2010**, *132*, 1273−1275.
(53) Rinaldo, D.; Philipp, D. M.; Lippard, S. J.; Friesner, R. A. *J. Am. Chem. Soc.* **2007**, *129*, 3135−3147.
(54) Gherman, B. F.; Baik, M.-H.; Lippard, S. J.; Friesner, R. A. *J. Am. Chem. Soc.* **2004**, *126*, 2978−2990.
(55) Song, W. J.; McCormick, M. S.; Behan, R. K.; Sazinsky, M. H.; Jiang, W.; Lin, J.; Krebs, C.; Lippard, S. J. *J. Am. Chem. Soc.* **2010**, *132*, 13582−13585.
(56) Bochevarov, A. D.; Li, J.; Song, W. J.; Friesner, R. A.; Lippard, S. J. *J. Am. Chem. Soc.* **2011**, *133*, 7384−7397.
(57) Senn, H. M.; Thiel, W. *Angew. Chem., Int. Ed.* **2009**, *48*, 1198−1229.
(58) Rulíšek, L.; Solomon, E. I.; Ryde, U. *Inorg. Chem.* **2005**, *44*, 5612−5628.
(59) Srnec, M.; Ryde, U.; Rulíšek, L. *Faraday Discuss.* **2011**, *148*, 41−53.